

# Experimental and numerical investigations on the process quality and microstructure during induction heating assisted incremental forming of Ti-6Al-4V sheet

Li, Weining; Attallah, Moataz; Essa, Khamis

DOI:

[10.1016/j.jmatprotec.2021.117323](https://doi.org/10.1016/j.jmatprotec.2021.117323)

License:

Creative Commons: Attribution-NonCommercial-NoDerivs (CC BY-NC-ND)

*Document Version*

Peer reviewed version

*Citation for published version (Harvard):*

Li, W, Attallah, M & Essa, K 2022, 'Experimental and numerical investigations on the process quality and microstructure during induction heating assisted incremental forming of Ti-6Al-4V sheet', *Journal of Materials Processing Technology*, vol. 299, 117323. <https://doi.org/10.1016/j.jmatprotec.2021.117323>

[Link to publication on Research at Birmingham portal](#)

## General rights

Unless a licence is specified above, all rights (including copyright and moral rights) in this document are retained by the authors and/or the copyright holders. The express permission of the copyright holder must be obtained for any use of this material other than for purposes permitted by law.

- Users may freely distribute the URL that is used to identify this publication.
- Users may download and/or print one copy of the publication from the University of Birmingham research portal for the purpose of private study or non-commercial research.
- User may use extracts from the document in line with the concept of 'fair dealing' under the Copyright, Designs and Patents Act 1988 (?)
- Users may not further distribute the material nor use it for the purposes of commercial gain.

Where a licence is displayed above, please note the terms and conditions of the licence govern your use of this document.

When citing, please reference the published version.

## Take down policy

While the University of Birmingham exercises care and attention in making items available there are rare occasions when an item has been uploaded in error or has been deemed to be commercially or otherwise sensitive.

If you believe that this is the case for this document, please contact [UBIRA@lists.bham.ac.uk](mailto:UBIRA@lists.bham.ac.uk) providing details and we will remove access to the work immediately and investigate.

# **Experimental and numerical investigations on the process quality and microstructure during induction heating assisted increment forming of Ti-6Al-4V sheet**

## **Abstract**

The conventional single point incremental forming (SPIF) process is unable to perform high geometrical accuracy and formability for the Ti-6Al-4V alloy sheet. In response, this article has proposed a reliable high-frequency induction heating-assisted SPIF system. Rapid localised heating (600 °C and 700 °C) was integrated with a synchronized Inconel 625 Nickel alloy ball-roller forming tool to achieve high geometric accuracy and surface quality. This article also produced new insights into correlating mechanical and microstructural properties in SPIF at 600 °C and 700 °C. By investigating the mechanical properties (forming force, geometric accuracy, thickness profile), an explicit finite element (FE) simulation was established to predict the results. The output strain history from the FE simulations was used as input and integrated with electron backscatter diffraction (EBSD) and micro-hardness characterisations, to form a constitutive model (Arrhenius model) to calculate the Zener-Hollomon parameter (Z-parameter). The grain size and micro-hardness experimental results were correlated with Z-parameter calculation to predict the microstructural development at the initial, middle, and final stages of the deformation process. The mechanical results revealed that the 700°C experiment performed enhanced geometric accuracy and thickness profile, with a reduced forming force. However, the surface quality is reduced as the lubricant dissipated rapidly, while the ball-roller tool effectively compensated for this behaviour by reducing the friction. At the microstructural level, 600°C revealed strong strain hardening and grain deformation, and 700°C revealed better grain refinement by dynamic recovery (DRV) and dynamic recrystallisation (DRX). A proportional relationship between Z parameters and grain size and a low-high-low micro-hardness profile was proposed.

**Keywords:** Hot Single Point Incremental Forming, Deformation behaviour, Finite Element analysis, Recrystallisation, Constitutive model, Zener-Hollomon parameter, Micro-hardness

## 1. Introduction

Ti-6Al-4V alloy has been widely used in aviation, automotive and medical industries, on account of its advantageous properties such as high strength, service temperature, and corrosion resistance. However, the deformation of Ti-6Al-4V remains a challenge. SPIF is a highly flexible computer numerical control (CNC) controlled sheet metal forming process that is efficient for relatively low strength materials at room temperature. For instance, ([Kumar et al., 2019](#)) reported excellent forming quality of aluminium alloy sheets. Further, ([Duflou et al., 2018](#)) studied the state-of-the-art of current SPIF methods and stated that the heating source should be integrated with the system to deform high-strength materials. In recent years, heat-assisted SPIF systems have been developed to deform high-strength alloy sheets. [Ambrogio et al. \(2017\)](#) have created an induction heating-assisted SPIF system that can deform the Ti-6Al-4V sheet at a temperature above 600 °C. Using the same heating method, ([Al-Obaidi et al., 2016](#)) obtained excellent geometric accuracy when deforming 22MnB5 steel at 750 °C. This article successfully applied thermomechanical behaviour on high-strength materials that induced material microstructural recrystallisation, which resulted in the reduction of material anisotropy. Thus, there are new challenges to study the heating method and subsequent microstructure characterisation to understand the mechanical behaviour of the materials in the SPIF process.

In previous work, laser heating assisted SPIF was reported by ([Göttmann et al., 2012](#)). A high-power laser heating system was used to deform a 1.5 mm thickness Ti-6Al-4V sheet. The laser is well-positioned to provide precise localised heating on the workpiece. However, the laser heating produced a strong heating track on the workpiece surface, and the apparatus setup is complicated, incurring a high cost and requiring extra safety measures. Alternatively, ([Xu et](#)

al., 2016) introduced the electric heating-assisted SPIF system, where a high-voltage direct current (DC) transformer generates the heat with the electric flux spread through the entire workpiece to make the material ductile. However, the spread of electric flux resulted in geometrical inaccuracy and adverse surface quality. Recently, (Ambrogio et al., 2017) have developed an induction heating assisted SPIF system where the heating coil is positioned underneath the sheet; with a connection to the forming tool, accurately localised heating is generated in the material from the centre to the outer surface. Thus, both geometrical accuracy and surface quality can be achieved by such a heating method. In this article, an induction heating-assisted SPIF system has been developed to provide rapid and accurate localised heating to deform the Ti-6Al-4V workpiece.

To reveal the relation between mechanical and microstructure behaviours, (Shrivastava and Tandon, 2018) studied the microstructural development of magnesium under SPIF. Experimentally measured mechanical properties and FE simulation obtained strain history were used to correlate the microstructural development. However, no attention has been given to apply this to heat-assisted SPIF especially for high strength materials such as Ti-6Al-4V. Thus, this article aims to build a heat-assisted SPIF system to address the above challenge.

In summary, to develop an economical, efficient, and high-accuracy SPIF system for Ti-6Al-4V alloy, a featured induction heat-assisted SPIF system has been developed. The mechanical and microstructural behaviours of Ti-6Al-4V for 600°C and 700°C were investigated. To correlate the mechanical and microstructural behaviours, FE simulations were established to verify the experimental results and to develop a constitutive model to estimate the microstructural development and deformation behaviour.

## 2. Material and methods

### 2.1. Experimental setup

To deform the Ti-6Al-4V alloy sheet, a high forming force is required during the process. The conventional tool tip may cause fractures and wear tracks on the workpiece surface due to the high friction force. A ball-roller tool tip forming tool was developed in this article, as shown in **Figure 1**. The tool shank was made of stainless steel with a 10 mm diameter IN 625 nickel alloy ball-roller as the tool tip. To cool down the forming tool, the tool shank has a hollow inner structure that increases the thermo-expansion on the tool tip. [Iseki and Naganawa \(2002\)](#) first introduced the ball-roller tool tip to improve the geometric accuracy of a conventional Incremental Sheet Forming (ISF) process. [Liu et al. \(2016\)](#) have optimized the ball-roller tool design and applied it in electric heat-assisted SPIF of Ti-6Al-4V workpiece of up to 500 °C. In the present work, IN 625 nickel alloy ball-roller was first applied and investigated for its reliability for induction heating SPIF.

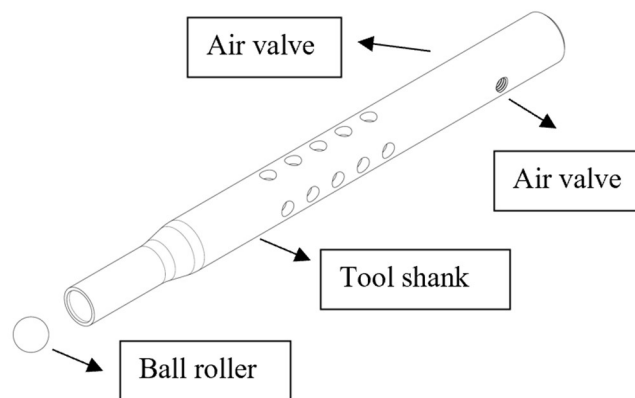


**Figure 1.** Design of ball-roller forming tool.

The induction heating SPIF system setup can be viewed in Figure 2(a-e). The main induction heater has a high frequency (900 KHz) alternating current (AC) inductor with a maximum power of 6.6 KW. The heat generation is obtained through the electromagnetic field that penetrates the workpiece to generate a rapid eddy current to heat the workpiece from inner to

outer surfaces. The heating coil diameter is 10 mm with three turns, which can provide maximum and accurate localised heating. The temperature can be maintained constant, with an error of 2% for a minimum heating process of 20 hours. A flexible support fixture was designed to hold the heating head to allow the synchronized movement between the heating coil and the forming tool in XYZ directions (Figure 2[a]). A mini 50kN low profile diaphragm load cell (Figure 2[b]) was fixed on the top of the forming tool to measure the reaction force during the process. The heating coil and forming tool setup were shown in Figure 2(c). The instantaneous temperature of the forming tool tip is measured by an infrared thermo-couple fixed on the forming tool holder by flexible support (Figure 2[d]), which has a measurement range from 400 °C to 1200 °C.

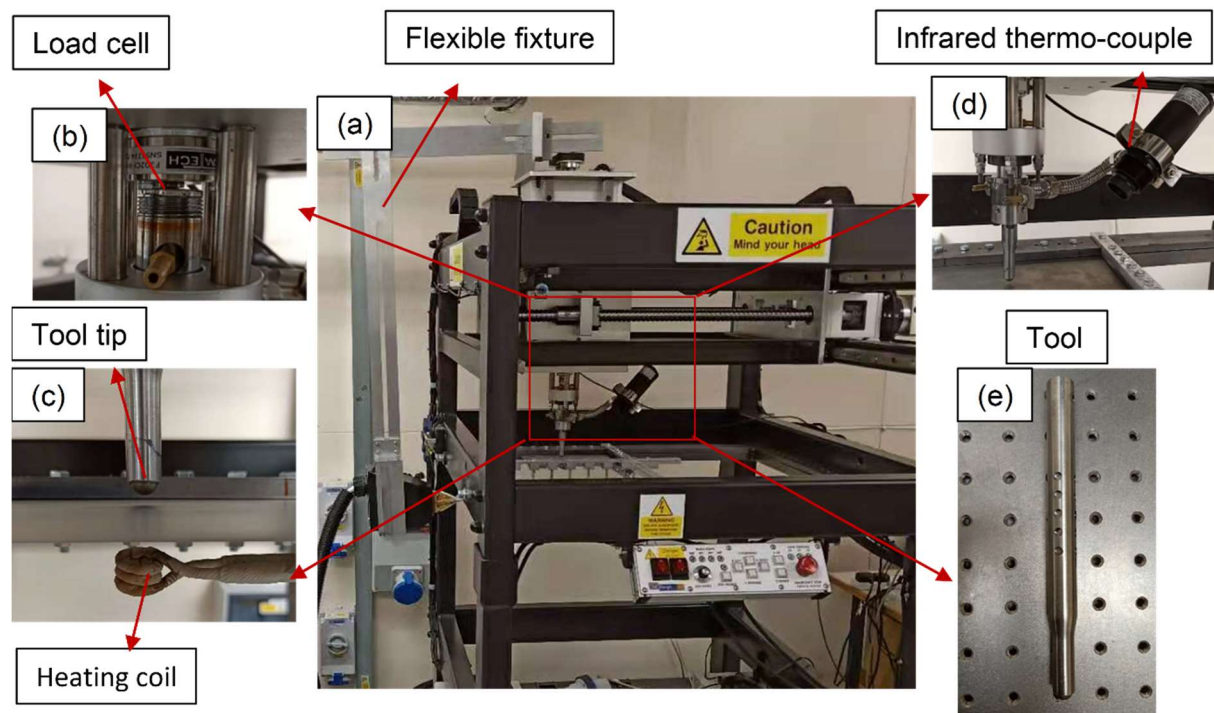


**Figure 2.** Overview of the induction heat-assisted SPIF system (a) flexible support fixture (b) load cell (c) forming tool-workpiece working scheme (d) infrared thermo-couple (e) forming tool.

## 2.2. Material and process parameters

### 2.2.1. Materials

A standard  $\alpha$ - $\beta$  class Ti-6Al-4V alloy sheet was chosen as the workpiece, with a size of 150 mm  $\times$  150 mm and a thickness of 0.8 mm. The chemical composition of the used Ti-6Al-4V alloy is shown in Table 1.

A heat-resistant liquid MoS<sub>2</sub> lubricant spray was used in this project to penetrate the specimen surface for even fits. According to the product datasheet, this lubricant is functional up to 600 °C.

**Table 1.** Chemical composition of Ti-6Al-4V

<b>Ti</b>	<b>Al</b>	<b>V</b>	<b>C</b>	<b>O</b>	<b>N</b>	<b>H</b>	<b>Fe</b>
<b>Balanced</b>	5.3	3.8	0.1	0.2	0.05	0.01	0.3

### 2.2.2. CAD model and process parameters

The final shape is a truncated cone that has a 100 mm major diameter, 30 mm height, and 45° wall angle as shown in Figure 3. The tool path was generated by Matlab, and a G-code was obtained from the Matlab coordinates output file to control the CNC machine. The detailed parameters and working temperatures are listed in Table 2. From the initial testing of 600 °C and 700 °C induction heating assisted SPIF, it can be seen in Figure 4 that the temperature rise at the initial stage is usually lower (around 30°C) than the set temperature, since time is taken (around 30 s) for heat generation to acquire steady-state. The steady-state temperature has a variation of  $\pm 2$  °C. When the process progresses to the last stage (final 40-60 s), the recorded temperature is slightly higher (around 30 °C) than the set as the whole workpiece has been subject to consecutive hot deformation. This is because the high-frequency heat transfer and

rapid tool movement associated with the process may result in re-heating behaviour that indicates higher readings.

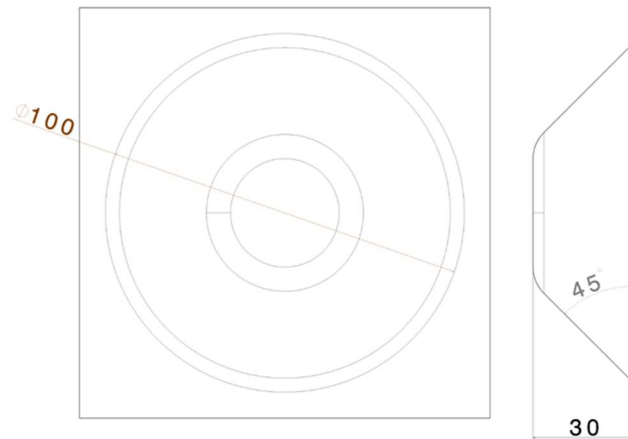


**Figure 3.** The dimensions of truncated cone to be made by induction heating assisted SPIF.

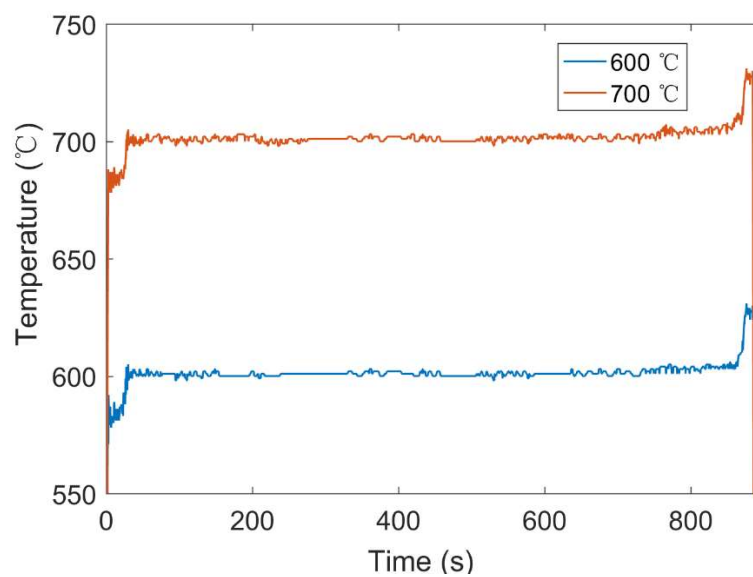


**Figure 4.** Measured temperature history for SPIF at 600 °C and 700 °C.

**Table 2.** Experimental parameters

EXPERIMENTAL PARAMETERS	TARGET TEMPERATURE (700 °C)	TARGET TEMPERATURE (600 °C)
----------------------------	--------------------------------	--------------------------------



Feed rate (mm/min)	1000	1000
Step size	0.5	0.5
Power (kW)	5.5	5.0
Frequency (kHz)	650	650

### 3. Finite Element Modelling

Abaqus CAE was used in this project for FE modelling of the induction heating-assisted SPIF process. The forming tool is considered an analytical rigid body with a pitch diameter of 10 mm. The dimension of the workpiece is 150 mm × 150 mm, with a thickness of 0.8 mm. The mechanical and thermal properties are provided by the Ti-6Al-4V alloy supplier. The details are represented in Table 3 and Table 4.

**Table 3.** Mechanical properties of Ti-6Al-4V

Temperature (°C)	YOUNG'S MODULUS (GPA)	POISSON'S RATIO	DENSITY (KG/M <sup>3</sup> )
25	113	0.33	4420
600	65.5	0.33	4336
700	55.5	0.33	4324

**Table 4.** Thermal properties of Ti-6Al-4V

Temperature (°C)	CONDUCTIVITY (W/M°C)	EXPANSION	HEAT CAPACITY (J/KG°C)
---------------------	-------------------------	-----------	---------------------------

25	7	$8.9 \times 10^{-6}$	546
600	14.2	$1.03 \times 10^{-5}$	673
700	15.5	$1.05 \times 10^{-5}$	694

### 3.1. Johnson-Cook (J-C) model

A J-C model was established to achieve a valid FE model using experimental data and assumptions from the literature. A flow stress prediction was produced with the application of the J-C model final equation and later compared with the literature for validation purposes. The constitutive equation of J-C model can be presented using the following equation:

$$\sigma = [A + B(\bar{\epsilon}^{pl})^n] \left( 1 + C \ln \frac{\dot{\bar{\epsilon}}^{pl}}{\dot{\epsilon}_0} \right) \left[ 1 - \left( \frac{T - T_r}{T_m - T_r} \right)^m \right] \quad (1)$$

Where  $\sigma$  is the yield stress,  $\bar{\epsilon}^{pl}$  is the equivalent plastic strain,  $\dot{\bar{\epsilon}}^{pl}$  is the equivalent plastic strain rate,  $\dot{\epsilon}_0$  is the reference strain rate,  $T$  is the working temperature,  $T_r$  is the room temperature,  $T_m$  is the melting temperature,  $A$  is the yield stress at reference strain rate and temperature,  $B$  is the coefficient of strain hardening,  $C$  is the coefficient of strain rate strengthening,  $m$  is the thermal softening coefficient, and  $n$  is the strain hardening exponent.

#### 3.1.1. Determination of material constants

By assuming that the reference temperature and strain rate is equivalent to the working temperature and plastic strain rate, the J-C can be simplified as:

$$\sigma = A + B(\bar{\epsilon}^{pl})^n \quad (2)$$

By applying natural logarithm on both sides, Eq. (2) can be expressed as:

$$\ln(\sigma - A) = \ln B + n \ln \dot{\epsilon}^p \quad (3)$$

To validate the J-C model predicted, specific constant values were obtained from the literature and set as input values in the J-C model calculation. By referencing the study by (Xu et al., 2020) on DRX of Ti-6Al-4V, the reference temperature  $T_r$  can be considered as 293 K and the melting temperature  $T_m$  can be considered as 1660 K. Since the working mechanism of the ISF process is governed by the complex stress and strain distribution in the forming area, common materials processing maps are not representative of the process. However, it is useful to obtain a strain rate from the literature that is close to the experiments in this article and to use it to validate the J-C model formation. The study by (Gatea et al., 2019) investigated the effect of forming parameters on the pure titanium ISF process, wherein the experiments indicate that the strain rate varies from  $0.01 \text{ s}^{-1}$  to  $0.08 \text{ s}^{-1}$  depends on the feed rate and wall angle. Another study by (Desalegn et al., 2019) has commented that the strain rate increases according to the increase of temperature in warm SPIF of aluminium alloy, where the range of strain rate varies  $0.01 \text{ s}^{-1}$  to  $0.1 \text{ s}^{-1}$ . In this article, the strain rate is set as  $\dot{\epsilon}_0 = 0.01 \text{ s}^{-1}$  which agrees with previous studies on ISF processes. The results can be validated with a processing map provided by the literature by (Nemat-Nasser et al., 2001), who studied the deformation behaviour of Ti-6Al-4V for a wide range of temperatures and strain rates. Other J-C model constants are obtained from (Kotkunde et al., 2014). These constants values were verified in the study by (Lee and Lin, 1998) on hot deformation of Ti-6Al-4V and (Wang et al., 2015) on J-C modelling of Ti-6Al-4V alloy.

Assuming a constant reference strain rate and temperature, Eq. (3) can be expressed as:

$$\sigma = [A + B(\bar{\epsilon}^{pl})^n] \left( 1 + C \ln \frac{\dot{\bar{\epsilon}}^{pl}}{\dot{\epsilon}_0} \right) \quad (4)$$

The constant  $C$  can be obtained from the gradient from the plotting of  $\ln[1 - \sigma/(A + B(\bar{\epsilon}^{pl})^n)]$  and  $\ln \frac{\dot{\bar{\epsilon}}^{pl}}{\dot{\epsilon}_0}$ .

Assuming a constant working temperature and reference strain rate, hence Eq. (4) can be expressed as:

$$\ln[1 - \sigma/(A + B(\bar{\epsilon}^{pl})^n)] = m \ln \left( 1 - \frac{T - T_r}{T_m - T_r} \right) \quad (5)$$

The constant  $m$  can be obtained from the gradient from the plotting of  $\ln[1 - \sigma/(A + B(\bar{\epsilon}^{pl})^n)]$  and  $\ln \left( 1 - \frac{T - T_r}{T_m - T_r} \right)$ .

The J-C model can be expressed as:

$$\sigma = [880.5 + 689.2(\bar{\epsilon}^{pl})^{0.35}] \left( 1 + 0.009 \ln \frac{\dot{\bar{\epsilon}}^{pl}}{\dot{\epsilon}_0} \right) \left[ 1 - \left( \frac{T - T_r}{T_m - T_r} \right)^{0.85} \right] \quad (6)$$

The determined material constants are represented in Table 5.

**Table 5.** Material constants for Ti-6Al-4V

A (MPa)	B (MPa)	C	n	m	$\dot{\epsilon}_0$ (s <sup>-1</sup> )
880.5	689.2	0.009	0.35	0.85	0.01

### 3.1.2. Flow stress behaviour validation and characterisation

To validate the J-C model, the predicted flow stress behaviours were compared with experimental flow curves obtained by (Nemat-Nasser et al., 2001) (at room temperature [RT],

526.85 °C, and 726.85 °C). In the present investigation, a similar range of temperatures and strain rates were used. As shown in Figure 5, the J-C model predicted flow behaviours agreed with the previous study.

It can be seen from Figure 5 that the flow stress is sensitive to temperature when the strain rate is constant. Additionally, the flow stress at RT is increasing rapidly according to the increase of strain at the initial stage (strain: 0 - 0.05), which indicates that rapid work hardening takes place. The behaviour is less pronounced for 526.85 and 726.85 °C. The previous study by (Xia et al., 2020) on the isothermal hot deformation of Ti-6Al-4VRu reported that the rapid increase of DRV at the initial stage is the main reason that causes the sharp increase in flow stress at low temperatures. During the DRV process, the rearrangement and removal of dislocations in the deformed grains' crystal structure led to their stored energy reduction and a sharp increase in the yield strength. The sharp increase is reduced as the temperature increases due to the DRX. The temperature increases the energy at grain boundaries until a critical value is reached. The recrystallisation takes place and induces a dynamic softening on the materials, thus healing the DRV. By observing Figure 5, a clear peak is present at 700 °C that indicates an occurrence of DRX, which softens the sharp increase by DRV.

Please note that the comparison of flow stress behaviour is used to validate the J-C model to prove its accuracy to simulate the induction heating SPIF process.

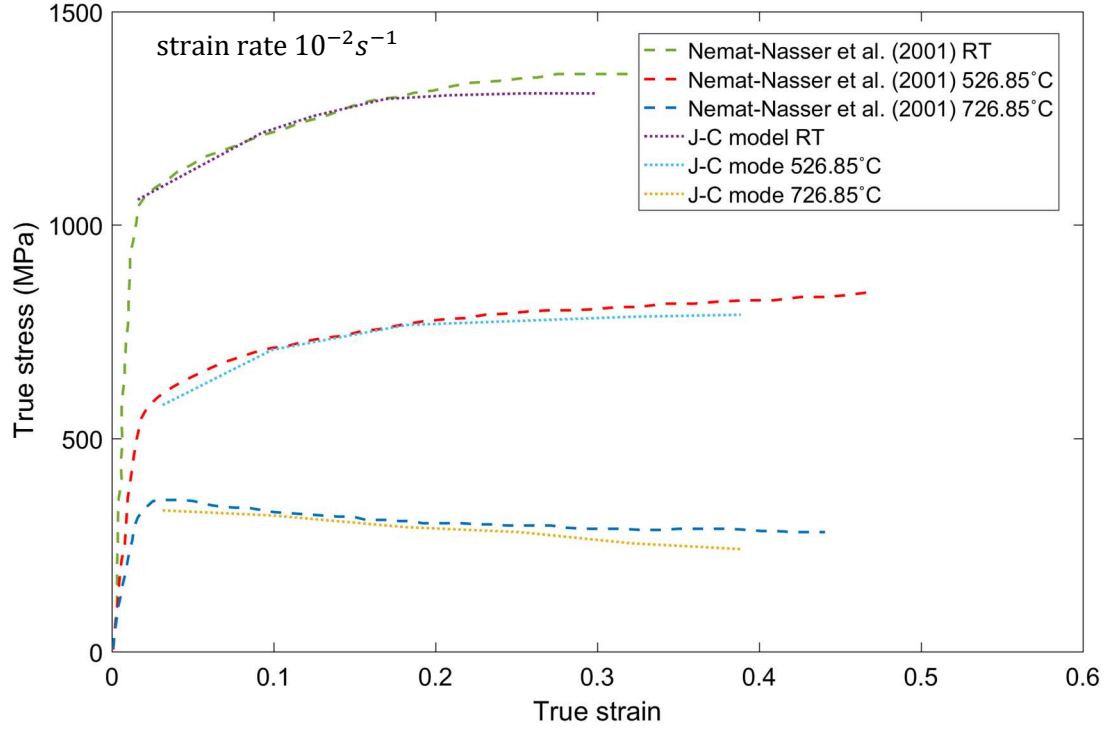


**Figure 5.** True stress-strain curves comparison between the literature and J-C models.

### 3.2. FEM processing

The induction heating SPIF can be expressed as a dynamic and temperature-displacement simulation in ABAQUS CAE. Coupled temperature - displacement explicit regime is used for process simulation. Since explicit analysis requires a large number of elements, mass scaling has been used to reduce the computational time. In this article, several mass scaling factors ranging from 100-100000 were used to test the reliability of the FE model. A workstation equipped with 20 Intel® Xeon® CPUs of 3 GHz and 120 GB ram was used to run the FE simulations. To ensure that the model is close to quasi-static and reduce the effect of mass scaling on the prediction accuracy, the kinetic energy should not exceed 10% of the maximum internal energy, as reported in the literature by (Essa and Hartley, 2009) and (Huang et al., 2008). Figure 6(a) shows the distributions of internal energy (ALLIE), kinetic energy (ALLKE), and artificial strain energy (ALLAE) at different mass scaling factors. Please note the simulations results are represented at 600 °C as an example. From Figure 6(b), it can be noticed

the ALLKE and ALLAE for all mass scaling factors did not exceed 10% of ALLIE which proves the reliability of the FE model. The effects of mass scaling on forming force and computational time are shown in Figure 6(b). It can be seen that mass scaling factors of 100000 and 75000 show less computational time (8 h and 20 h), but poor prediction accuracy of the forming force. When the mass scaling factor is reduced to 50000 or less, the prediction accuracy is close to the experimental result, with a reasonable computational time of 48 h. Please note that the data in Figure 6(b) were smoothed using the Savitzky-Golay filter method in the Matlab plot toolbox.

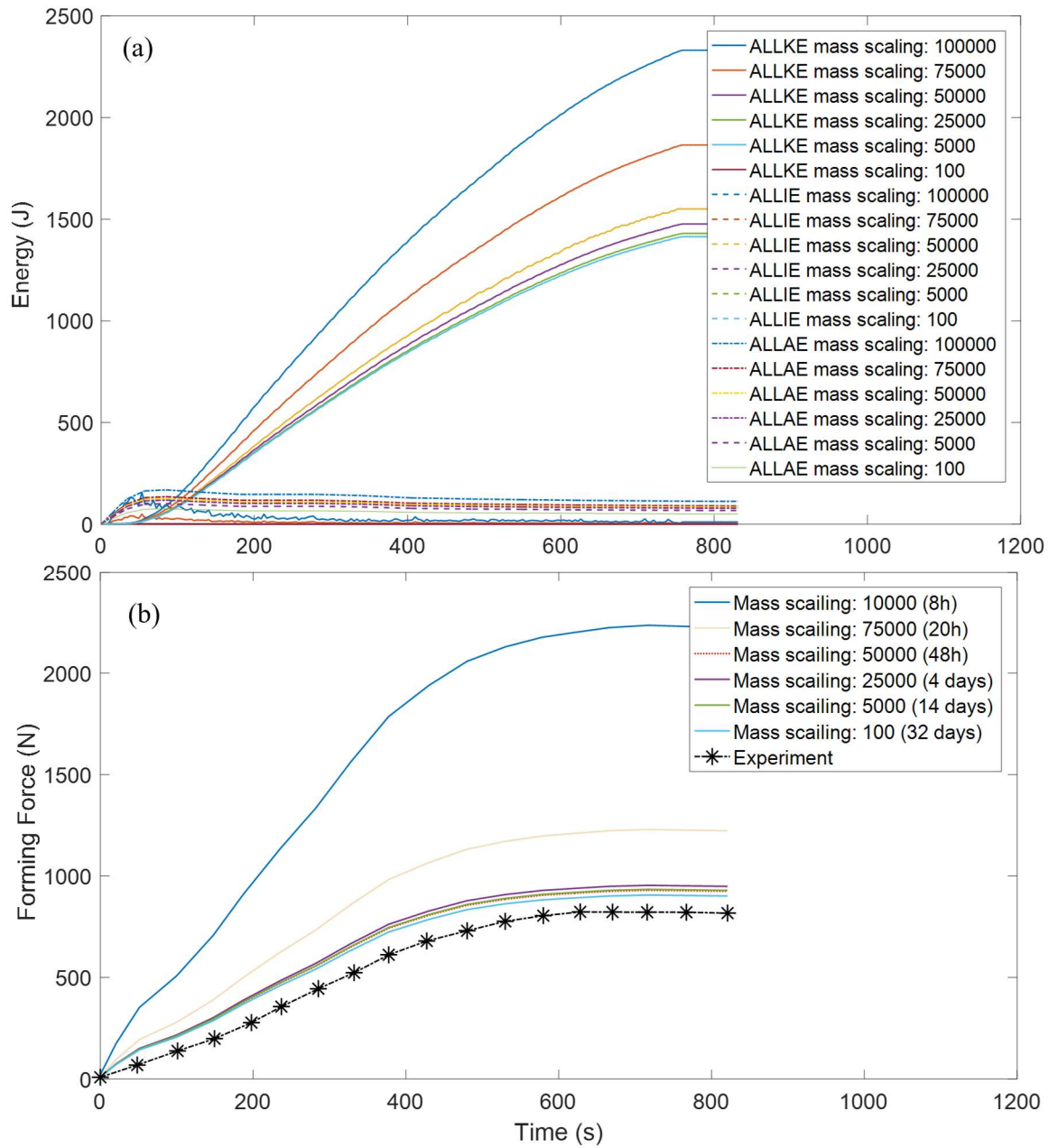


**Figure 6.** FE modelling of SPIF at 600 °C using different mass scaling factors (a) energy history (b) forming force.

The interaction between workpiece and tool was defined as a surface-to-surface contact with Tangential behaviour. A friction value of 0.1 was set in the model; this value was obtained from the previous study by (Gatea et al., 2017) on the modelling of ductile fracture in SPIF, based on Coulomb's friction law calculation. The friction model and value have been further verified with the study by (Honarpisheh et al., 2015) on hot SPIF simulation. The four edges



of the workpiece were constrained using displacement boundary conditions where  $U_x = U_y = U_z = 0$ , and the tool was defined as a rigid body. The boundary conditions setting followed the general SPIF modelling conditions reported by (Essa and Hartley, 2011). The same FE conditions setting and experimental setup has been verified in another previous study by (Moser et al., 2016) on the FE modelling of double-side ISF. Two temperature boundary conditions (600 °C and 700 °C) are set for the forming tool to simulate different experimental environments. Since the experiments recorded a temperature variation at the initial and final stages, a 30 °C temperature variation has been applied to the first 30 s (-30 °C) and final 50s (+30 °C) of tool path movement amplitude to compensate for the error in temperature history. The element selected for the FE analysis is 8-node thermally coupled brick, trilinear displacement, and temperature (C3D8T) which is most applicable for this analysis. A total of 7200 elements are applied to the workpiece with an approximate global size of 0.0025 and a maximum deviation factor of 0.1.

#### **4. Geometrical, surface, and material characterisation**

##### **4.1. 3D geometric scanning**

Geometric accuracy is a significant factor that reveals the overall performance and quality characteristics of parts made by the SPIF process. The FARO Edge-scan 8-Axis laser 3D Scanning Arm was used in this study to obtain the 3D cloud of points of deformed parts. The resolution of this system is 40 µm, with a measurement error of  $\pm 0.2$  µm. Geomagic was then used to process the cloud of points and obtain a highly accurate measurement of the final profile and thickness distribution.

##### **4.2. Surface roughness**

Surface roughness is the most common measure to represent the surface quality of the forming parts. Alicona Infinite Focus is a highly accurate optical 3D surface measurement system to

measure the surface roughness of the as-received and deformed samples. This machine is equipped with various optical microscopes which enables it to provide precise 3D surface data with a vertical resolution of 50 nm, minimum measurable roughness of 0.03  $\mu\text{m}$  and measurement error of 2%. 401MVD Vickers micro-hardness tester is used in this article to provide high accurate micro-hardness results of the as-received and deformed samples with a measurement error of 0.5%.

### **4.3. SEM**

A benchtop SEM JOEL 6000 was used in this project to analyse the microstructure of the as-received and deformed samples. The images can be taken at magnifications from 20x to 50,000x with an accelerating voltage of 15 kV. All SEM samples were mounted, and chemical-mechanical polishing with 0.04  $\mu\text{m}$  Colloidal Silica (OP-S) suspension was used. Etching was performed on each sample using Kroll's reagent (2 ml HF, 10 ml HCl, 88 ml H<sub>2</sub>O) to provide a more pronounced microstructure.

### **4.4. EBSD**

Philips XL-30 was used in this article for grain growth analysis. This instrument was fitted with an Oxford Instruments INCA EDS system and an HKL EBSD system with a Nordlys camera. The camera utilized 100% 1344  $\times$  1024 pixels resolution and a rapid 8  $\times$  8 pixels binning. The obtained data were analysed with HKL CHANNEL 5 software to perform microstructural characterisation.

The EBSD data were collected with the following information: every slice at a step size of 0.07  $\mu\text{m}$ , the pixel binning mode was set as 2  $\times$  2, and the accelerating voltage was 30 kV with an electron beam current of 5 nA.

#### **4.5. Micro-hardness**

Wilson® hardness tester was used in this project to provide high accurate hardness results of the as-received and deformed samples. The measurements follow GB/T 4340.1-2009 HV 0.1 metal hardness testing standard with a testing load of 100 gm. The machine reading error is 0.5%.

### **5. Results and discussion**

#### **5.1. Forming force**

A comparison between simulation and experimental forming force at 600 °C and 700 °C is shown in Figure 7(a-b). For the experimental results, there is a surface-to-surface contact between the workpiece and forming tool at the initial experimental setup, with a variation of 50 N - 80 N is applied on the workpiece. For the simulation results, an ideal initial situation was assumed wherein the forming force is 0 N at the starting point of the process. It is important to note that the data are filtered by the Savitzky-Golay method to remove the frequency noise.

As illustrated in Figure 7(a-b), experimental and simulation forming forces are agreed upon from the beginning to the steady-state region. Since the strain rate for these two experiments remains almost constant, the temperature dominates the forming force trendline. At 600°C, the temperature is relatively low to induce pronounced DRV and DRX, and the strain hardening and grain deformation form a strong micro-texture which induces the high forming force. At 700 °C, the pronounced grains slip and dislocation results in better DRV and DRX to form an enhanced grain refinement, which leads to a relatively isotropic microstructure that reduces the forming force. This agrees with the study by ([Davarpanah et al., 2015](#)) on microstructural properties of SPIF on polymers. The study reported that at room temperature strain-induced deformation and recrystallisation lead to anisotropic microstructure, while cycle heating results in enhanced recrystallisation that leads to isotropic properties. Another study by ([Bantounas et](#)

[al., 2009](#)) on the investigation of grain orientation of Ti-6Al-4V shows that a better grain refinement can be achieved by increasing the temperature at a constant strain rate, which proves that both temperature and strain rate have effects on recrystallisation results. Additionally, the study by ([Guan et al., 2018](#)) on FE simulation of high-speed machining of Ti-6Al-4V reported that common hexagonal close packed (HCP) crystal materials favour the shear band induced local-strain recrystallisation that occurs at heat treatment. High forming force is required for strain hardening induced deformation texture at low temperature. Conversely, the heat treatment on Ti-6Al-4V induces shear band strain to HCP crystals that form an enhanced recrystallised texture.

By comparing the experimental and simulation results, it can be demonstrated that an excellent agreement has been achieved. The collected raw data shows strong fluctuation towards the end of the deformation process. Data filtering may result in little deviation at the regions with high fluctuation, which explains the negligible difference between simulation and experimental results at the end of the forming process. Besides, lubricant dissipation towards the end of the process may lead to a change in the friction coefficient which affects the forming force. [Hussain et al. \(2008\)](#) has investigated the malfunction of lubricant in SPIF of Titanium alloy. The study reported that adherence of the workpiece material on the tool may lead to unpredictable failures on the workpiece, thus affecting the deformation process. Further, a study by ([Fan et al., 2010](#)) revealed that the temperature variation during the SPIF process could lead to local springback which could significantly affect to the deformation process.

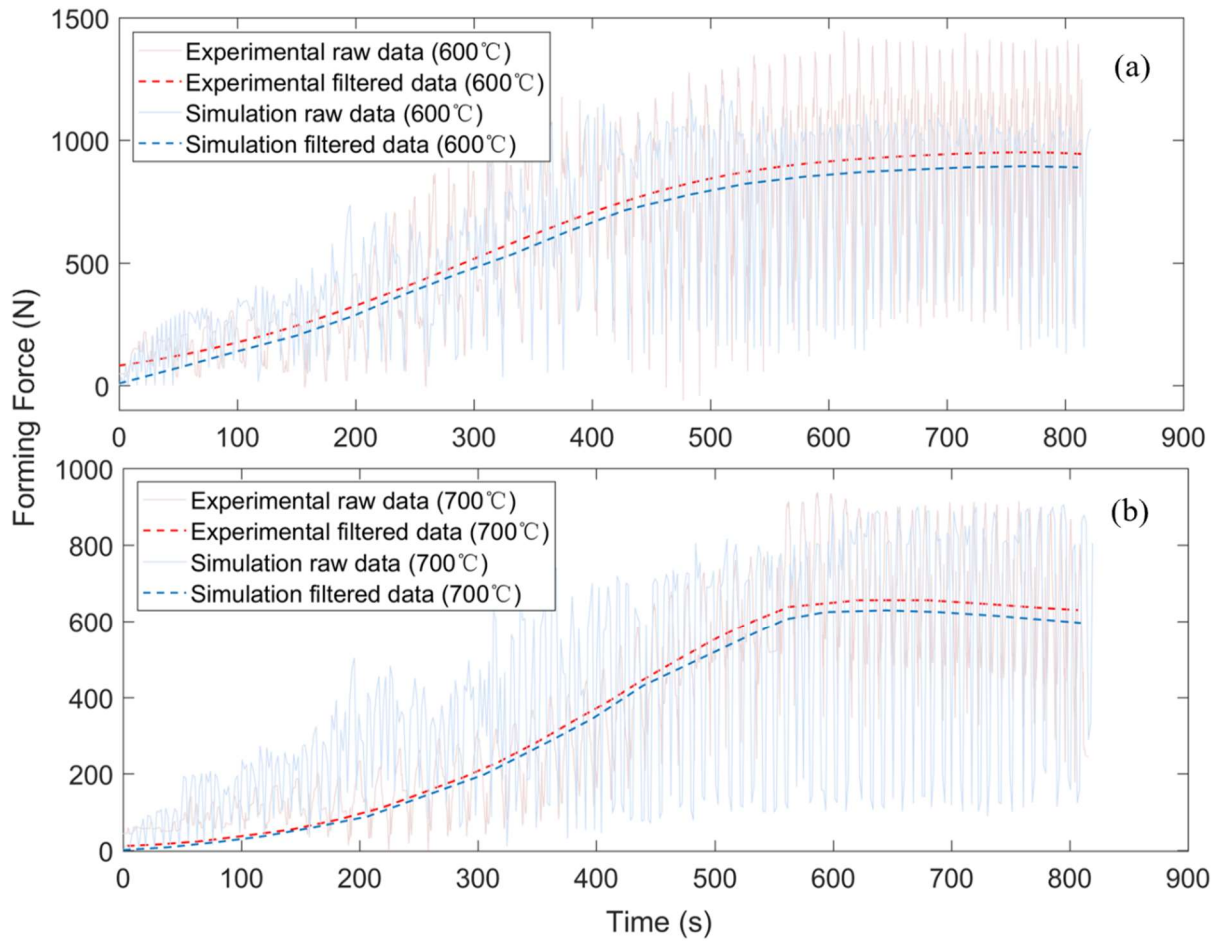


**Figure 7.** Comparison of forming forces between experimental and FE simulation at (a) 600 °C (b) 700 °C.

## 5.2. Geometric profile

The FE profile of the workpiece formed at 600 °C, and 700 °C as well as the experimentally measured profile are shown in Figure 8(a-b). A path from the workpiece edge to the centre was obtained from the FE model to demonstrate the FE profile data. It is important to note that the experimentally measured profiles were obtained using FARO 3D scanning on the clamped workpiece to match the displacement boundary conditions applied in the FE simulation. This prevents any errors from unclamping and cooling to reveal the impact of introducing the induction system. If rapid localised heating is transferred to the workpiece precisely, the experimentally measured profile should agree with the FE simulation.

As illustrated in Figure 8(a-b), only slight springback at the cone base and pillow effect at the cone centre were measured before unclamping. Still noticeable, the successful application of rapid localised heating has enhanced the deformation process. Hence, it can be concluded that induction heating assisted SPIF can deform Ti-6Al-4V with high geometric accuracy. The measured profile at 700 °C shows excellent agreement with the FE profile compared with that at 600 °C. This can be attributed to the enhanced recrystallisation-induced microstructure that results in a reduction in springback and pillow effects. This is a typical phenomenon that occurs in hot SPIF as the thermomechanical behaviour may induce high residual stress and stress relaxation in the material which results in springback and pillow effects. Similar observations were also reported in a previous study by (Ortiz et al., 2019) on the geometric accuracy of the hot SPIF process.

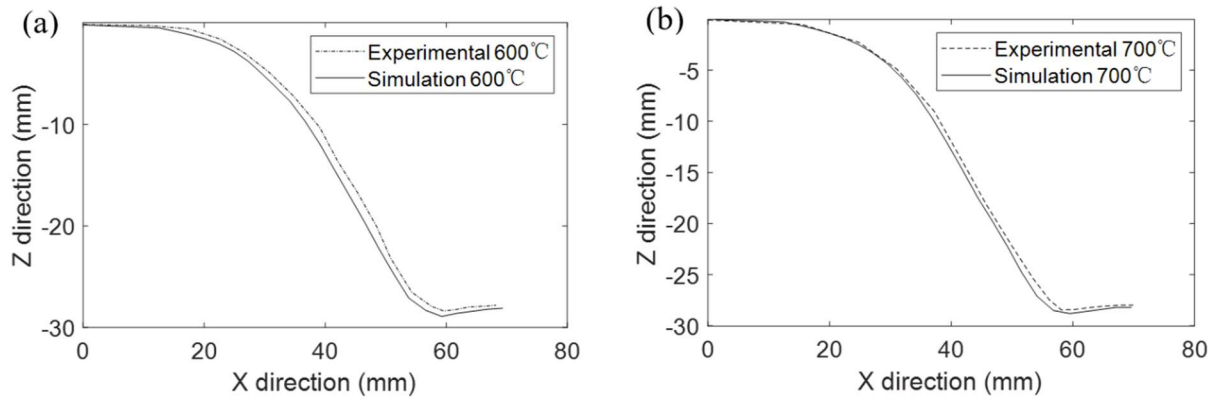


**Figure 8.** Comparison between FE and experimental profile at (a) 600 °C and (b) 700 °C.

### 5.3. Thickness distribution

Figure 9 and Figure 10 illustrate the thickness distributions measured from the sheet edge to its centre at 600 °C and 700 °C, respectively. The sheet thickness of FE simulation can be obtained using Eq. (7), and the theoretical thickness distribution can be obtained from the sine law as shown in Eq. (8). Cao et al. (2015) studied the ISF process and reported that the sine law is efficient to predict the thickness distribution of deformed parts. The experimental thickness (X,

Y, Z displacement) was obtained using the FARO 3D scanner for two paths, with one path on the upper surface and the other one on the lower surface of the deformed workpiece.

The sheet thickness can be calculated by the following equation:

$$t = \sqrt{(x_1 - x_2)^2 + (y_1 - y_2)^2 + (z_1 - z_2)^2} \quad (7)$$

Where  $t$  is the sheet thickness,  $x_1, y_1, z_1$  are the coordinates of nodes on the top surface path,  $x_2, y_2, z_2$  are the coordinates of nodes on the lower surface path.

The theoretical thickness distribution can be obtained by applying cosine law as the following equation:

$$t_f = t_0 \sin \theta \quad (8)$$

Where  $t_f$  is the final thickness of the workpiece,  $t_0$  is the initial thickness of the workpiece,  $\theta$  is the wall angle. This equation was proposed in the previous study by (Hussain and Gao, 2007) to estimate the thickness distribution in SPIF. Lu et al. (2015) applied the same principle to predict the theoretical thickness of double-side ISF. Another study by (Tolipov et al., 2019) on multi-point forming also verified its efficiency to estimate the thickness distribution in sheet metal forming.

From Figure 9(a-b), it can be seen that the sheet thinning is proportional to the cone depth. The sine law predicted sheet thinning of 0.565 mm for a 45° wall angle. As illustrated, the maximum sheet thinning remains constant from 30 mm to 50 mm at X-direction along the cone wall. At 600 °C, the experimentally measured thickness distribution slightly outfits the one obtained from the FE simulation (from 0 mm to 20 mm at X-direction). This can be attributed to insufficient heat generation at the initial stage of the process. The rapid tool movements and insufficient temperature at this region (around 570 °C) initiated a strong DRV process that

induced high strain hardening, thus resulting in strong springback. Once the temperature acquired steady-state at 600 °C (from 20 mm onwards at X-direction), the experimentally measured thickness shows good agreement with the FE simulation. This phenomenon reveals good evidence of grains deformation that assists the material softening which leads to better agreement.

As shown in Figure 9(b), the experimentally measured thickness at 700 °C shows very good agreement with the FE simulation. At the initial stage (from 0 mm to 20 mm at X-direction), a slight outfit can be observed. This outfit is eliminated as the process progresses to the steady-state temperature region (from 20 mm onwards). This phenomenon reveals the presence of DRX initiated at the initial stage and then becoming more pronounced at the steady-state stage.

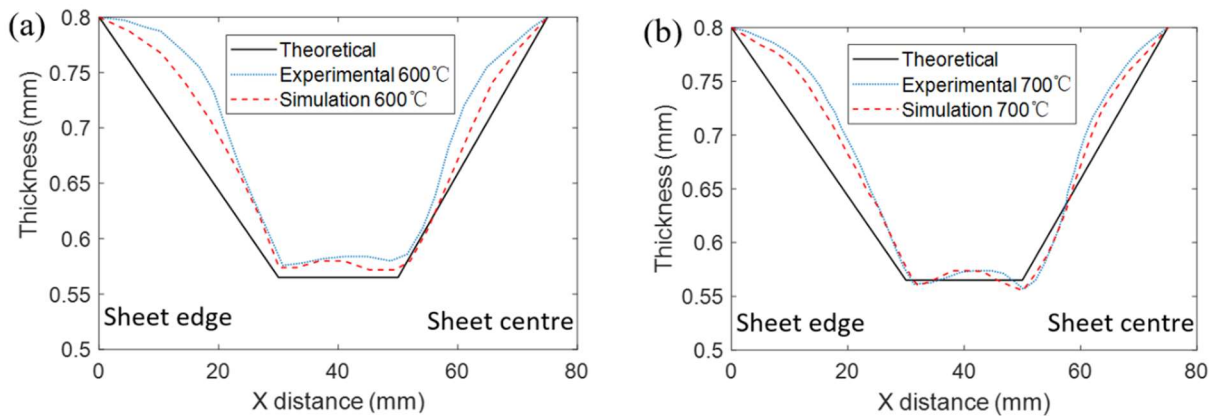


**Figure 9.** Comparison of thickness distribution obtained by the theoretical sine law, experiment and FE simulation (a) 600 °C, (b) 700 °C.

#### 5.4. Surface roughness

For each formed workpiece (600 °C and 700 °C), 3 sections (5 mm<sup>2</sup>) were cut off from the upper, centre, and lower parts for surface roughness measurement as shown in Figure 10(a-b). The 3D surface topography of each sample is represented in Figure 11(a-g). Figure 12 illustrates the average surface roughness ( $S_a$ ) of all samples, and Table 6 represents the root-



mean-square height ( $S_q$ ), maximum peak height ( $S_p$ ), maximum valley depth ( $S_v$ ), maximum height ( $S_z$ ) of each sample.

From the visual observation of results in Figure 10(a) and Figure 10(b), it can be seen that the surface quality at 600 °C is better than that at 700 °C. Only a limited number of wear tracks are observed on the 600 °C samples. The dark colour from the centre to the lower region can be attributed to the adherence of dried lubricant. Conversely, the 700 °C sample reveals obvious wear tracks from the upper until the lower region. Such a phenomenon can be attributed to the exorbitant temperature and rapid lubricant dissipation during the process. The lubricant service temperature is 600 °C; the exceeding working temperature may therefore cause lubricant malfunction. For effective operating condition, as in Figure 10(a), the upper region shows a smooth surface with limited wear tracks, which indicates functional lubricant. As the process progressed to the centre region, observable wear tracks occurred, and the material colour becomes darker incrementally. The phenomenon indicates a slow dissipation of the lubricant; the liquid lubricant transforms to a viscous state as the temperature increases. The rapid movement of the forming tool results in the formation of contaminated layers that adheres to the workpiece surface. By observing the surface of the 700 °C sample in Figure 10(b), it is worth noting that slight contamination (dark colour) can be observed at the centre region as the lubricant dissipation is more rapid even without any contamination being formed. The colour change of the 700 °C sample can also support the presence of recrystallisation. According to a previous study by (Ortiz et al., 2020) on hot SPIF of Ti-6Al-4V, the colour change appears when samples are heat-treated at 900 °C for 2h and indicates pronounced grains dislocation in the crystal, which is enhanced in the process. Another study by (Satko et al., 2016) on oxygen layer evolution in titanium microstructure reveals that an oxidation  $\alpha$ -case layer can be formed at long exposures (420 h) at a relatively low temperature (650 °C). Since the working temperature for this study is 700 °C, the colour change only reveals a sudden variation of

temperature when the tool leaves its position to the new path (ending and starting point of each path) throughout the process. The movement of forming tool in this region may result in limited oxidation as the temperature fluctuates around the set temperature.

From the 3D surface topography profile shown in Figure 11(a-g), it can be seen that the measurements of  $S_a$  between 600 °C and 700 °C SPIF process is in similar distribution. By comparing the details,  $S_a$  for SPIF at 700 °C is higher than 600 °C, this is evident that the dissipation of lubricant has an observed effect on the distribution of  $S_a$  along the SPIF process, however, there is no strong effect on the shape forming.

As illustrated in Figure 12. It is noticed that the values of  $S_a$  is increasing with the progressing of the SPIF process while lower values of  $S_a$  at 600 °C as compared with that at 700 °C. The previous study by ([Ambrogio et al., 2012](#)) on induction heating SPIF of Ti-6Al-4V using MoS<sub>2</sub> (the same lubricant used in this investigation), reported that the induction heating SPIF has better performance than electric heating and friction heating SPIF. In this article, the ball-roller tool tip has shown higher surface quality than the previous work. Please note that all data in this figure are filtered by the Gaussian filter for inclined planar surfaces to reduce the noise.

By investigating the measured amplitude parameters of each sample in Table 6, it can be observed that the  $S_q$  is following the same trend as  $S_a$ . This is evident that the friction is increasing while the lubricant dissipates. However, it is still noted that the  $S_z$  (difference between  $S_p$  and  $S_v$ ) of 600 °C and 700 °C samples are in converse trend. The upper region of 600 °C indicates higher values and the centre regions reveal relatively lower values, and the values are maintained in the lower regions. However, the opposite trend can be observed at 700 °C. This is clear evidence that the 600 °C at the upper region is insufficient and unstable to soften the material thus leads to a higher forming force that increases the  $S_z$  between each step. As the forming tool is progressing to the centre and lower region, the workpiece becomes soft

enough which leads to a reduction in  $S_z$ . While this phenomenon is insignificant at 700 °C since the temperature is sufficient to increase the ductility of the workpiece at the upper region, the measured  $S_z$  in the deformed samples is very small. As the forming tool is progressing to the centre and lower region of the workpiece, the dissipation of lubricant results in an increase of  $S_z$ , however, results are still lower than that at 600 °C. This phenomenon proves that the lower forming force at 700 °C improves the geometric accuracy while surface roughness can be improved if proper lubricant is used.

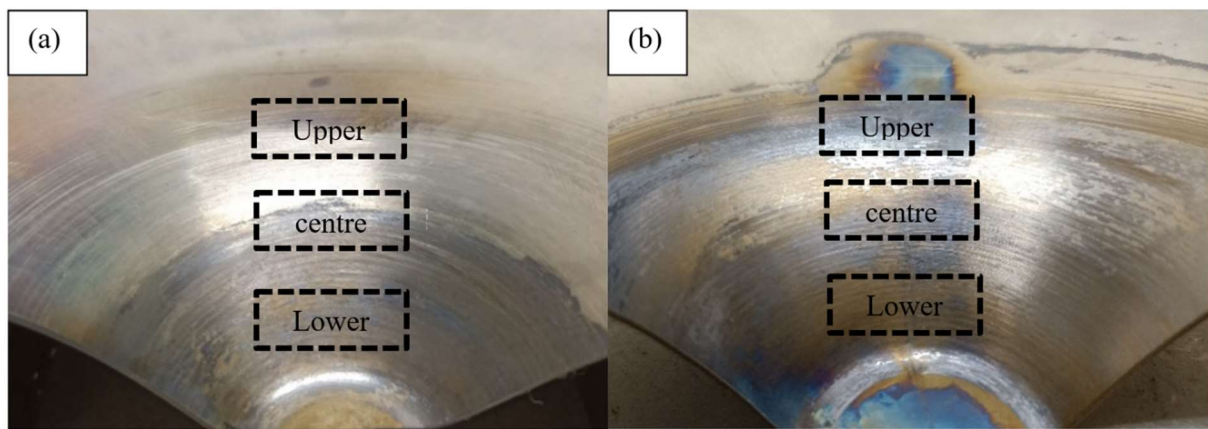


**Figure 10.** locations of collected samples for surface roughness measurements (a) 600 °C (b) 700 °C.

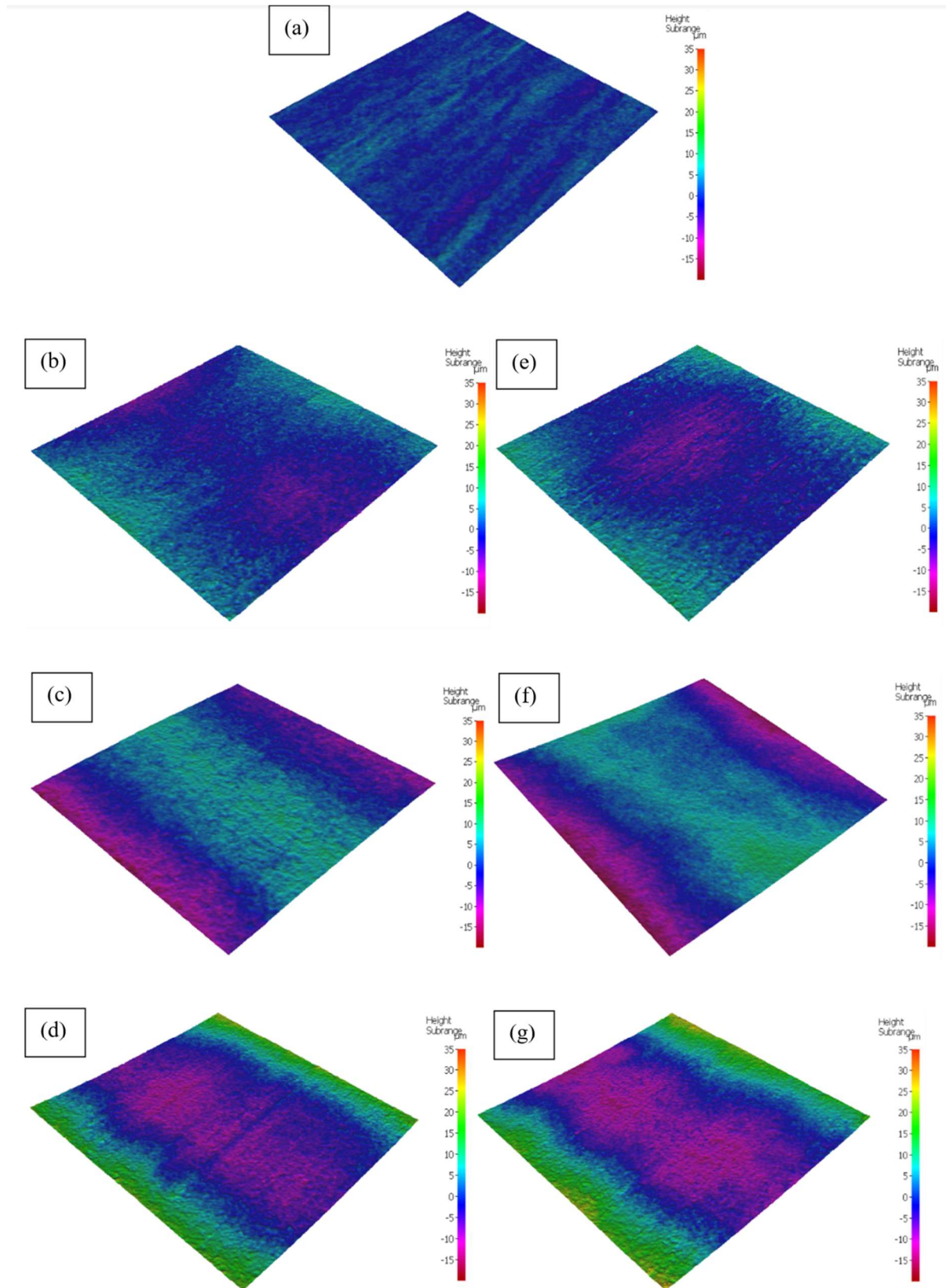


**Figure 11.** Surface roughness for (a) as-received (b) 600 °C upper region (c) 600 °C centre region (d) 600 °C lower region (e) 700 °C upper region (f) 700 °C centre part (g) 700 °C lower region.

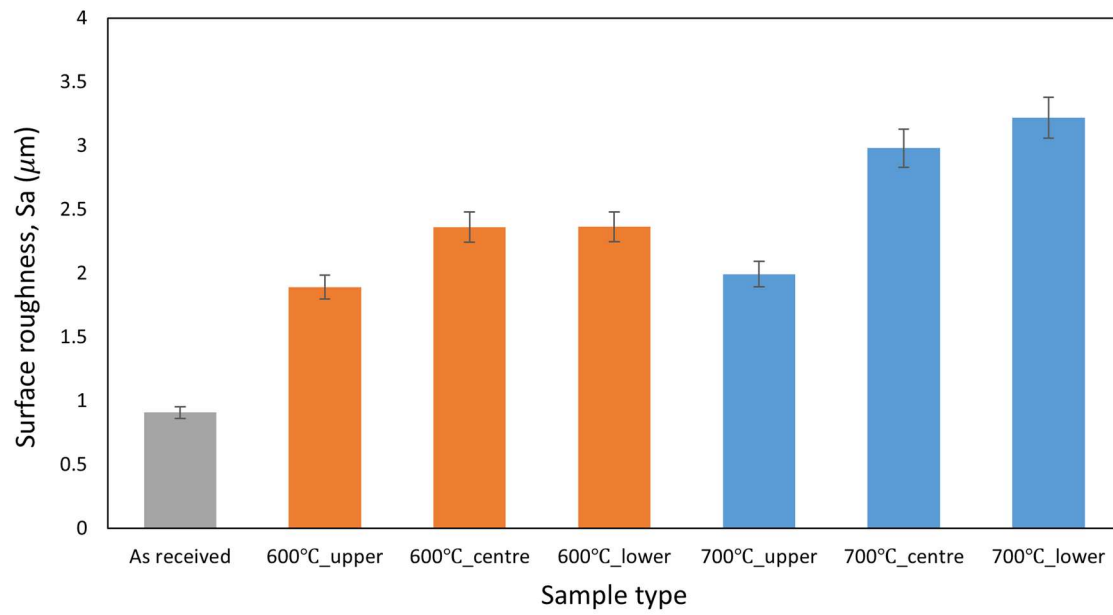


**Figure 12.** Filtered surface roughness histogram for different samples.

**Table 6.** Measured amplitude parameters of each sample

	$S_q$ ( $\mu\text{m}$ )	$S_p$ ( $\mu\text{m}$ )	$S_v$ ( $\mu\text{m}$ )	$S_z$ ( $\mu\text{m}$ )
As received	1.143	2.490	3.710	6.20
600 °C upper region	1.842	7.545	7.441	14.986
600 °C centre region	2.116	6.998	5.751	12.748
600 °C lower region	2.261	6.185	6.913	13.098
700 °C upper region	2.608	5.358	5.403	10.761
700 °C centre part	3.651	5.570	5.977	11.548
700 °C lower region	3.673	6.185	6.913	13.098

## 5.5. Microstructure analysis

### 5.5.1. SEM analysis

The microstructures of the lower region in the as-received, 600 °C and 700 °C samples are shown in Figure 13. As illustrated, the microstructure is mainly  $\alpha$  phase, the average  $\alpha$  grain size in the as-received SEM image (Figure 13[a]) is estimated to be 5  $\mu\text{m}$  – 10  $\mu\text{m}$  with random equiaxed grain shape. The intergranular  $\beta$  phase grains are detected at  $\alpha$  phase boundaries. A noticeable increase in finer  $\alpha$  grains is observed in Figure 13(b), and a pronounced increase of finer  $\alpha$  grains can be seen in Figure 13(c). As illustrated, the grain size of fine  $\alpha$  grains for 600 °C and 700 °C samples is reduced to 5  $\mu\text{m}$ . This can be considered as strong evidence that the grain refinement level increases as the temperature increases.

The previous study, reported by (Qu et al., 2018) on microstructural evolution and oxidation mechanisms of titanium alloy, reveals that titanium alloy exhibits excellent oxidation resistance at 700 °C. However, clear recrystallisation can be observed at this temperature. In the present study, it is worth noticing that the induction heating system successfully dominates the level of grain refinement at 600 °C and 700 °C, which supports the forming tool with a sufficient thermomechanical force to deform the workpiece.

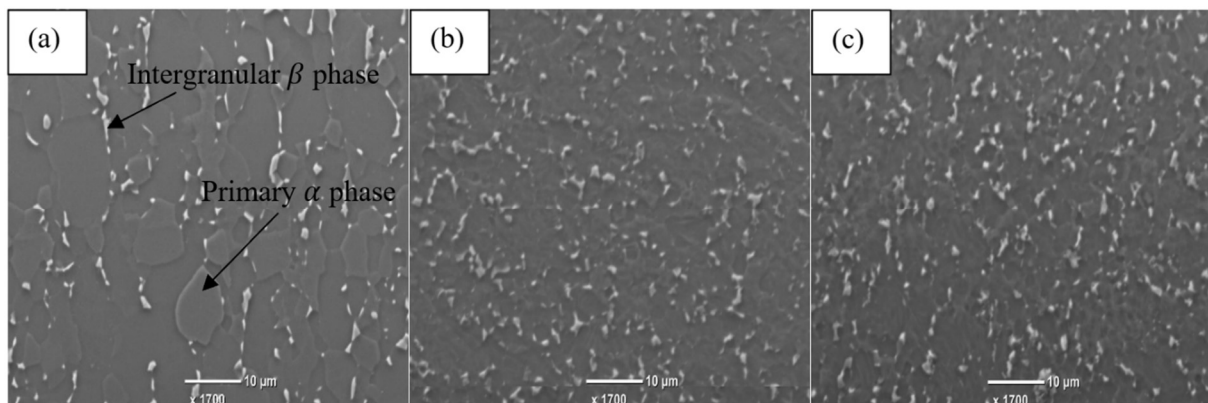


**Figure 13.** SEM images of (a) as-received sample (b) 600 °C sample (c) 700 °C sample.

### 5.5.2. EBSD analysis

To study the fraction of Ti-6Al-4V grain size changes and orientation after the hot SPIF process, EBSD was performed on each of the upper, centre, and lower region samples. Please note that only the lower region samples data were presented in this study since they have revealed the required information under the peak temperature and strain throughout the process. The EBSD scanning direction is the perspective of transverse direction (TD), which represents the in-depth (thickness direction) microstructure changes of the sample without the effects from the rolling manufacture process.

The lower region samples at 600 °C and 700 °C were obtained from EBSD examined inverse pole figure (IPF) maps, and are illustrated in Figure 14(a-c). The average grain size for all samples was calculated by EBSD post-processing software HKL Channel 5 and represented in Figure 15. Grain area ( $\mu\text{m}^2$ ) is selected to represent the average grain size as the scan area is relatively small with limited grain numbers. The average grain area is more representable than the average length ( $\mu\text{m}$ ) to distinguish the grain size difference.

As shown in Figure 14(a), the as-received sample exhibits a structure of coarse equiaxed grains of  $4.62 \mu\text{m}^2$  (Figure 15); no noticeable recrystallized grains can be observed from the figure. Conversely, the 600 °C revealed a significant difference as shown in Figure 14(b), notably, a pronounced increase of recrystallised finer grains is generated, and the average grain size is reduced to  $3.39 \mu\text{m}^2$  (Figure 15). However, the temperature is relatively low to induce significant DRV and DRX, which only results in a texture with the initiation of grains deformation. When the temperature increase to 700 °C, as in Figure 14(c), a pronounced growth of recrystallised finer grains can be observed at coarser grain boundaries, and the average grain size is reduced to  $1.44 \mu\text{m}^2$  (Figure 15). This is strong evidence that grain deformation and DRV can be initiated at low temperatures (600 °C) with high strain hardening, and a more completed DRV and DRX be achieved by increasing the temperature to 700 °C.



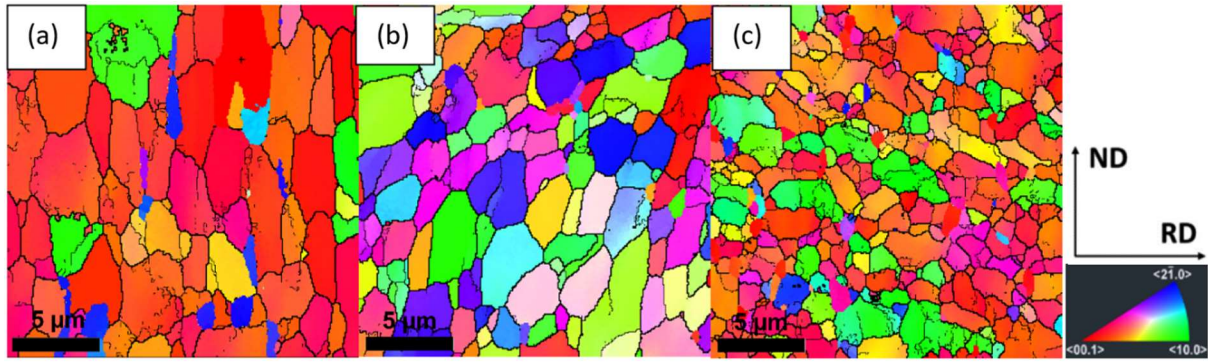


**Figure 14.** Microstructural evolution of as-received sample (a) IPF map with grain boundary distribution of as-received sample (b), IPF map with grain boundary distribution of 600 °C sample and (c) IPF map with grain boundary distribution of 700 °C sample.

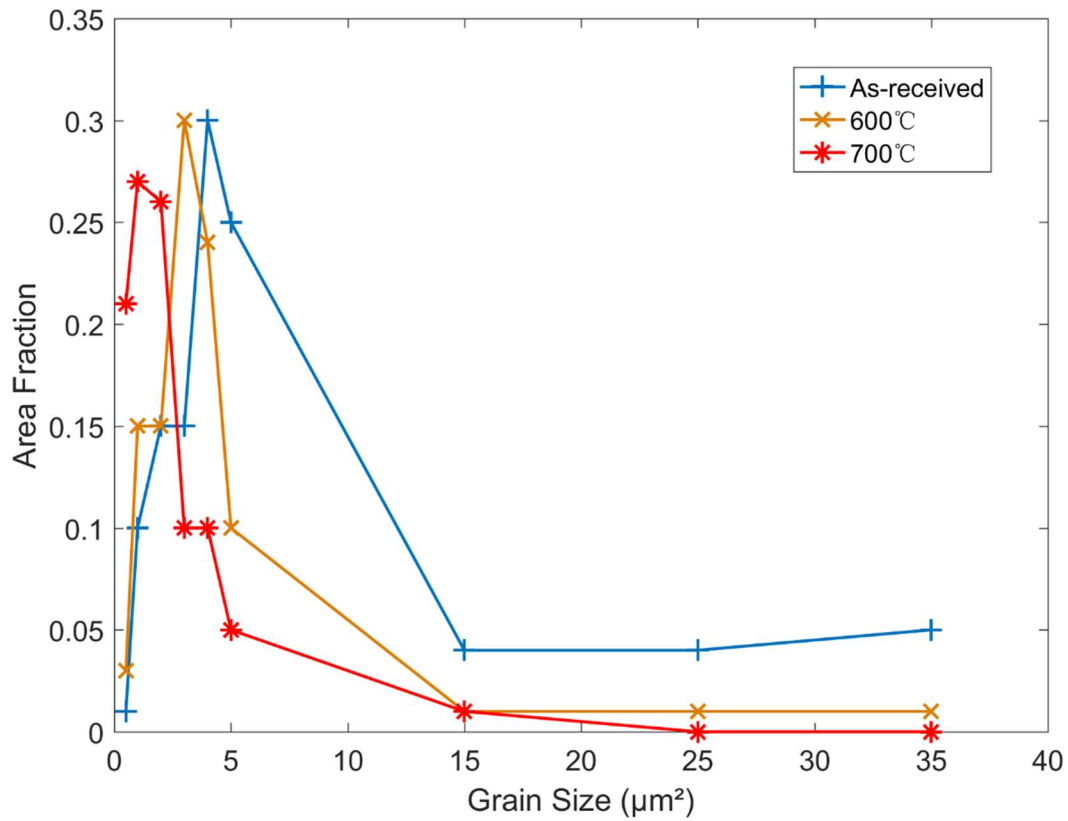


**Figure 15.** Grain size evolution (a) as-received sample, (b) 600 °C SPIF sample and (c) 700 °C SPIF sample.

The details of the misorientation angle distribution of IPF maps (Figure 14) are collected from HKL Channel 5 and statistically re-arranged using the Matlab Mtex toolbox which is created



by (Niessen et al., 2021) on the study of grain reconstruction from transformed microstructures, as shown in Figure 16. Notably, the as-received sample reveals a high percentage of low-angle grains ( $< 15^\circ$ ), while the percentage of high-angle grains ( $> 15^\circ$ ) is increased incrementally, with further temperature increasing and strain hardening. According to a study on SPIF of magnesium by (Shrivastava and Tandon, 2018), the low-angle grains ( $< 15^\circ$ ) commonly appear on the as-received sample and are transferred to high-angle grains ( $> 15^\circ$ ) on the deforming sample. Such a phenomenon is also a typical feature that reveals the presence of DRX on hot deformation of Ti-6Al-4V alloy, which is also observed in previous study by (Orozco-Caballero et al., 2018) on the ductility of  $\alpha$ -Ti under different temperatures. The study reported that the low-angle grains subject to deforming grains at low temperatures, the majority of them slip to recrystallised high-angle grains in high-temperature deformation, which provides a microstructure that makes the material ductile. Zherebtsov et al. (2016) have investigated the microstructure evolution of Ti-6Al-4V during low-temperature superplastic deformation, supported the previous conclusion and reported that the behaviour is more pronounced above  $650^\circ\text{C}$  as the temperature could initiate a better DRX process. In this article, the thermomechanical straining behaviour at  $700^\circ\text{C}$  accelerates the grain slip and dislocation that results in enhanced DRV and DRX. Thus, the misorientation angle increase is much higher than  $600^\circ\text{C}$ , where  $600^\circ\text{C}$  only represents a misorientation texture due to insufficient temperature. The study by (Wang et al., 2020), on grain refinement mechanism in Ti-6Al-4V alloy, states that the crystal texture of  $\alpha$ -Ti induces transformation if the grains slip from stable slip modes to active slip modes during hot deformation works. Therefore,  $700^\circ\text{C}$  in the present work provides sufficient temperature to support a constant incremental straining behaviour to the sample for full grains slip initiation.

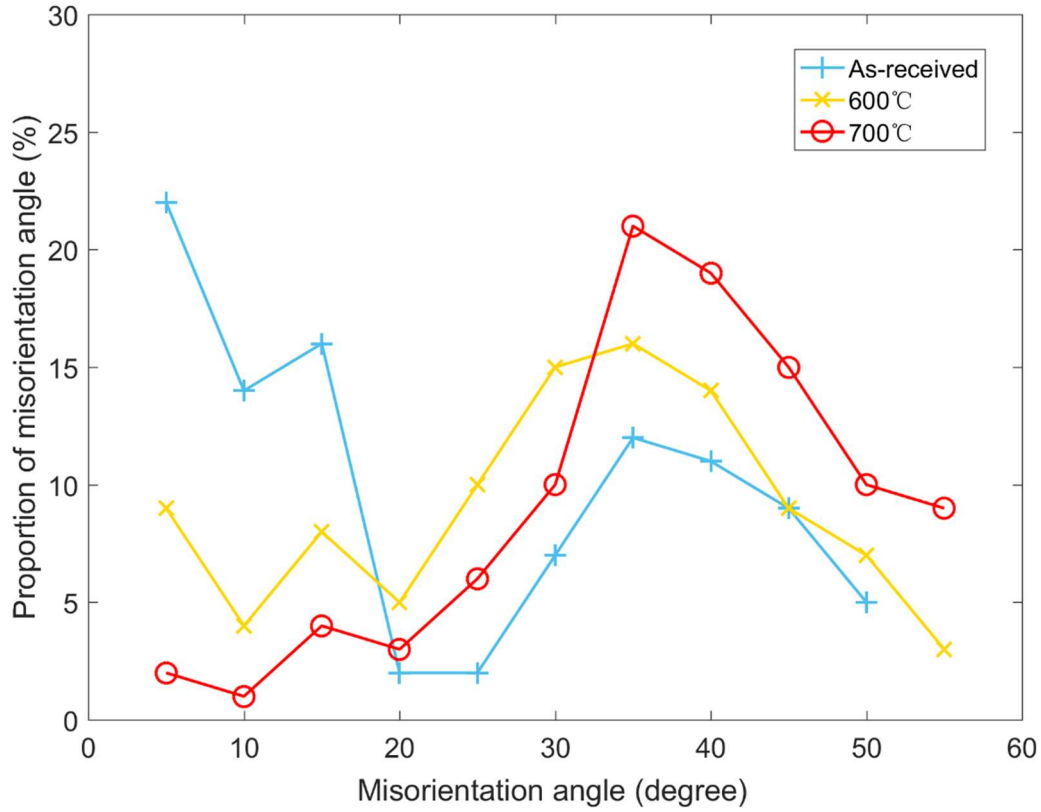


**Figure 16.** Misorientation angle distribution histogram of as-received, 600°C, 700°C samples.

### 5.6. Micro-hardness

The micro-hardness measurements are applied to the TD surface of each sample. The orientation of the indents was in a step-down arrangement which covers the measurements from the upper sample edge to the lower edge. Due to the sheet thinning in the experiment, only 5 indents can be applied to the deformed samples, where 9 indents were applied to the as-received sample.

As illustrated in Figure 17, the as-received sample indicates a high-low-high hardness distribution. Since the Ti-6Al-4V sheets being used in this article are manufactured by hot rolling, the surface has been heat-treated before manufacturing. Thus, it may result in slight oxidation on the surface. The previous study by (Dai et al., 2020) on microstructure and hardness of Ti-6Al-4V sheet surface under heat-treatment work, has reported that the average

hardness readings on the as-received sample surface are slightly higher than the centre region, which is due to the surface finishing process that induces thermal-strain. Such behaviour may results in limited oxidation that enhances the  $\alpha$ -stabilising of Ti-6Al-4V, thus increasing the hardness at the surface.

Conversely, the micro-hardness profile of all deformed samples (at 600 °C and 700 °C) illustrates a low-high-low distribution profile. Such behaviour can be attributed to the working mechanism of induction heating. In such a system, the magnetic field penetrates the workpiece that generates a rapid alternating eddy current at the centre material which is then spreading to the outer region. Thus, the highest thermomechanical strain will occur in the centre region. Such a phenomenon is a crucial factor that enhances the strain-hardening work from centre to edge. The previous study by ([Najafabady and Ghaei, 2016](#)) on the investigation of effects on the hardness of Ti-6Al-4V alloy by hot incremental forming, has reported that the strain hardening is pronounced at 600 °C, and it is effective in increasing the micro-hardness. Another study by ([Sabat et al., 2018](#)) on the texture and microstructure evolution of Ti-6Al-4V revealed that the strain hardening and grain deformation induce higher micro-hardness readings at 600 °C. However, the temperature is insufficient to generate the full DRV and DRX process. Thus, it results in the creation of a deforming microstructure, which is demonstrated by the presence of a strong deformation texture. Using a higher temperature of 700 °C accelerates the dislocation mobility and results in full DRV and DRX, which can be manifested in grain refinement, as shown in the EBSD measurements (Figure 15 and Figure 16).

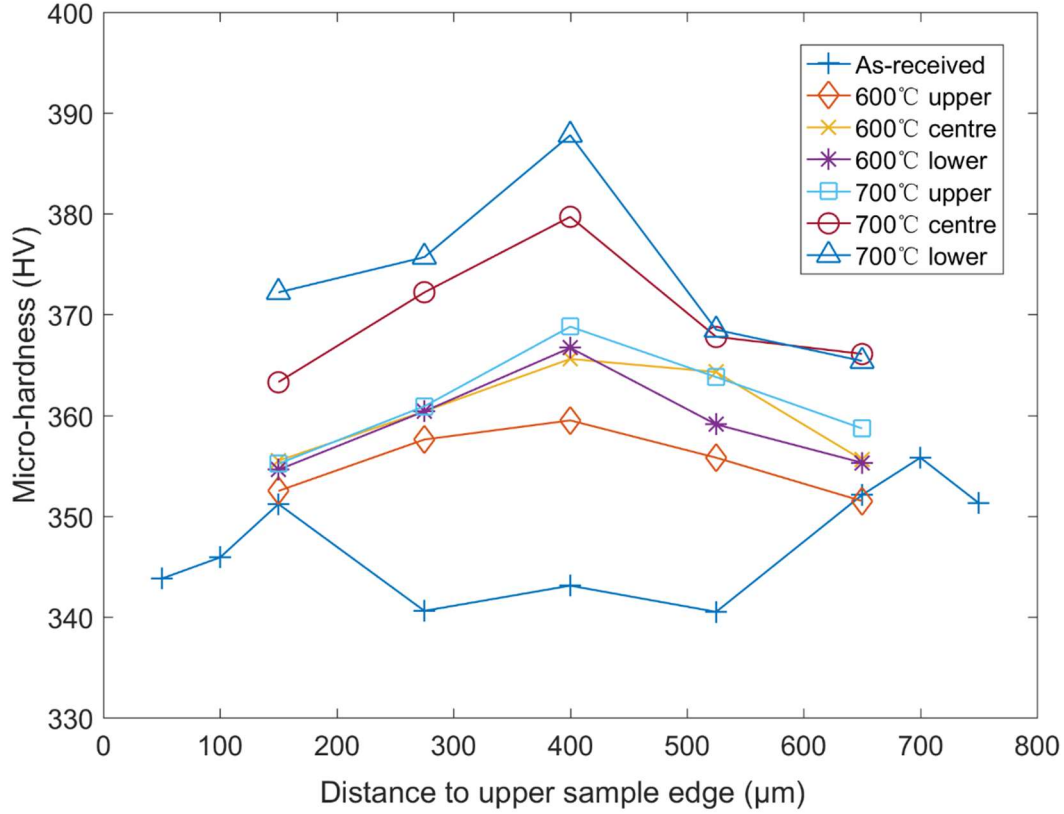


**Figure 17.** Micro-hardness profile distribution of all samples.

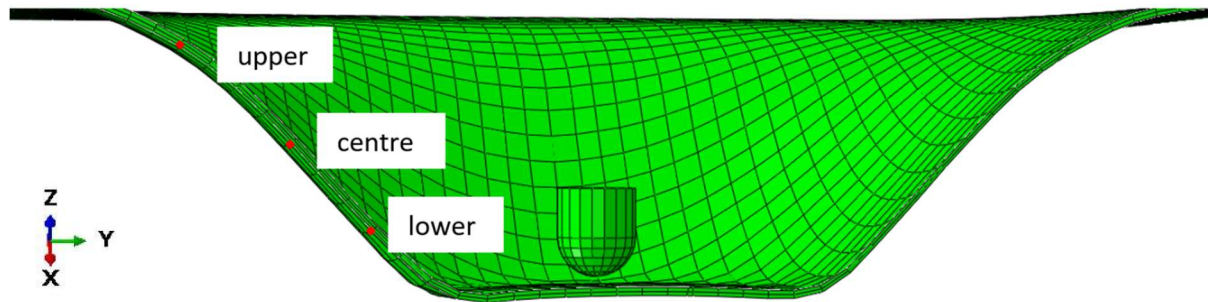
### 5.7. Calibration of Ziner-Hollomon parameter

To relate the mechanical properties (strain, strain rate) with microstructure evolution (grain refinement, hardness distribution), an Arrhenius type constitutive model has been established to demonstrate the relationship.

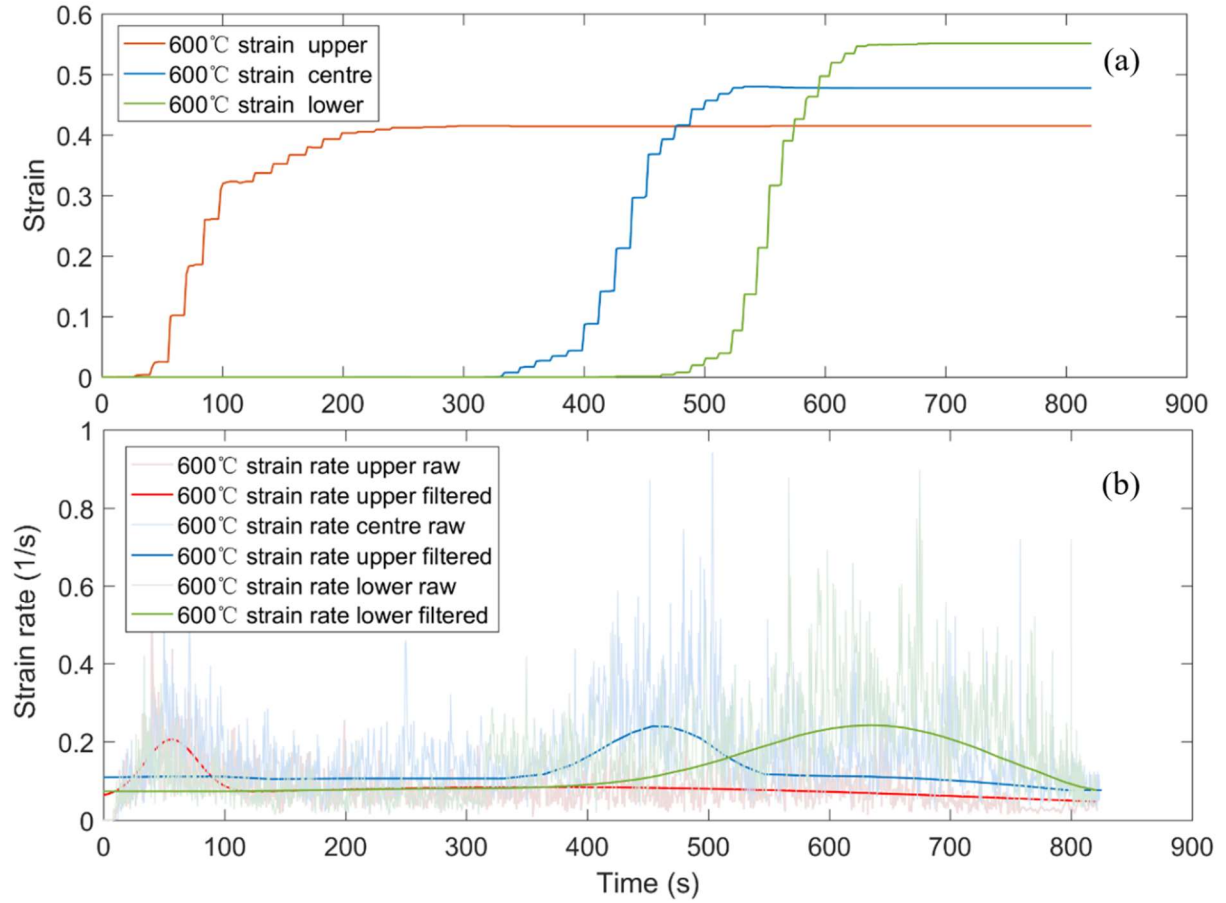
In this article, the samples are obtained from different positions (upper, centre, lower) of the deformed workpieces at different temperatures (600 °C, 700 °C). Three unique nodes from the FE model transverse direction (thickness direction) are selected to extract the raw data for these three positions as shown in Figure 18. The Savitzky-Golay filter method is used to reduce the frequency noise of the raw data.

Figure 19(a) represents the equivalent plastic strain for transverse direction and Figure 19(b) represents the strain rate for the 600 °C samples. The 700 °C samples are not illustrated as its

data closely resembles that at 600 °C, with an increase in values. It is worth noting that the equivalent strain distribution can be correlated with strain rate distribution through-thickness. As the forming tool passes through the unique node, the strain rate climbs the peak and induces an increase in equivalent strain. As stated in the previous study by (Smith et al., 2015) on the anisotropic yield criterion for pressure-dependent materials, hardening behaviour is sensitive to the equivalent plastic strain distribution, especially dependent on the rigid indenter displacement. In the SPIF process, each step-down increment stretches the surface of the workpiece and induces uniform thickness distribution. As the maximum thickness (between the centre and lower part) is achieved, the strain distribution tends to maintain its value.



**Figure 18.** Positions of the upper, centre, and lower nodes from the FE model.



**Figure 19.** FE history output for upper, centre, lower region (a) equivalent strain for SPIF at 600 °C (b) strain rate for SPIF at 600 °C.

To establish the Arrhenius model, the peak strain rate value and its corresponding equivalent strain value for the unique nodes are used for calculation. The 600 °C upper samples are used as an example, equivalent strain  $\approx 0.4$  and strain rate  $\approx 0.2 \text{ s}^{-1}$ .

The Arrhenius equation can be expressed as:

$$\dot{\epsilon} = AF(\sigma)\exp\left(-\frac{Q}{RT}\right) \quad (9)$$

Where  $\dot{\epsilon}$  is the strain rate, A is the material constant,  $\sigma$  is the flow stress, Q is the apparent activation energy, R is the gas constant (8.314 J/K mol), T is the experimental temperature (K).

The flow stress  $\sigma$  can be expressed as three conditions:

$$F(\sigma) = \begin{cases} \sigma^{n_1}, \alpha\sigma < 0.8 & \text{condition 1} \\ \exp(\beta\sigma), \alpha\sigma < 1.2 & \text{condition 2} \\ \sinh(\alpha\sigma)^n, \text{ for all } \sigma & \text{condition 3} \end{cases} \quad (10)$$

Where  $\alpha, \beta, n_1, n$  are material constants. Condition 1 represents the low-stress level; condition 2 represents the high-stress level; condition 3 includes all stress and strain level.

The strain rate for deformation can be produced by using the Zener-Hollomon parameter (Z-parameter). The equation can be expressed as:

$$Z = \dot{\epsilon} \exp\left(\frac{Q}{RT}\right) \quad (11)$$

Where  $Z$  is the Zener-Hollomon parameter,  $\dot{\epsilon}$  is the strain rate,  $Q$  is the apparent activation energy,  $R$  is gas constant (8.314 J/K mol), and  $T$  is the experimental temperature (K).

The material constants can be calculated by obtaining the gradients from the fitting equations by transforming Eq. (9) and considering condition 3 from Eq. (10). Where the constant  $n_1$  can be obtained from the gradient of plotting  $\ln\sigma - \ln(\dot{\epsilon})$ . The constant  $\beta$  can be obtained reciprocal of gradient from the plotting of  $\ln\sigma - \ln(\dot{\epsilon})$ . By substituting the calculated constants  $\beta$  and  $n_1$  into the equation  $\alpha = \beta/n_1$ ,  $\alpha$  can be calculated accordingly. The details of calculations and fitting graphs are not represented in this article to avoid distraction from the main objective here. The calculated material constants are represented in Table 7.

**Table 7.** Identification of material constants

Constants	$\alpha, \text{MPa}^{-1}$	$\beta$	$n_1$	$n$
600 °C	0.045	0.0012823	0.0281	29.128
700 °C	0.036	0.0012465	0.0350	35.831

Substituting the calculated constants to the fitting equations,  $Q_{600^{\circ}\text{C}} = 261.30 \text{ KJ/mol}$  and  $Q_{700^{\circ}\text{C}} = 321.43 \text{ KJ/mol}$ . The results of  $Q$  have been validated with studies (Tabei et al., 2017) on constitutive modelling of Ti-6Al-4V under hot deformation, (Weiss and Semiatin, 1999) on alpha titanium alloys under thermomechanical processing, and (Xiao et al., 2012) on constitutive modelling and microstructure changes of Ti-6Al-4V under hot tension.

Substituting  $Q_{600^{\circ}\text{C}} = 261.30 \text{ KJ/mol}$  and  $Q_{700^{\circ}\text{C}} = 321.43 \text{ KJ/mol}$  into Eq. (11), the equation can be expressed as:

$$Z = \begin{cases} Z_{600^{\circ}\text{C}} = \dot{\epsilon} \exp\left(\frac{261.30}{RT}\right) \\ Z_{700^{\circ}\text{C}} = \dot{\epsilon} \exp\left(\frac{321.43}{RT}\right) \end{cases} \quad (12)$$

## 5.8. Grain size vs. Z-parameter

To demonstrate the relation between grain size and Z-parameter, the grain size of the upper, centre, and lower samples was obtained from EBSD. By obtaining the strain rate values from the corresponding FE nodes from Figure 18, the Z parameter can be calculated using Eq. (12). By applying a natural logarithm on both sides of grain size ( $d$ ) and Z-parameter ( $Z$ ), the relationship is represented in Figure 20. It is important to note that labels 1,2,3 in the figure represent the upper, centre, and lower regions of the sample, respectively. Since the temperature supply at the upper region is insufficient, that leads to weak strain hardening and results in higher grain size. Once the temperature acquires a steady-state at the centre and lower region, the grain size is then reduced as better grains refinement is achieved.

It is worth noting that temperature and strain rate are key factors that motivate the grains dislocation microstructurally. An increase in temperature leads to accelerate dislocation process that results in the development of stress relaxation between the grains that enhance the DRX process. Thus, the grain refinement at  $700^{\circ}\text{C}$  is more pronounced than that at  $600^{\circ}\text{C}$ . A



study by (Ammouri et al., 2015) has investigated the grain size and Z-parameter relations of AZ31B alloy and reported a similar observation that the grain size is inverse-proportional to Z-parameter. This is attributed to the thermal activation in the material microstructure. The process increases the crystal dislocation which induces grain growth and refinement, results in low angle to high-angle grains transformation in the low Z-parameters zone.

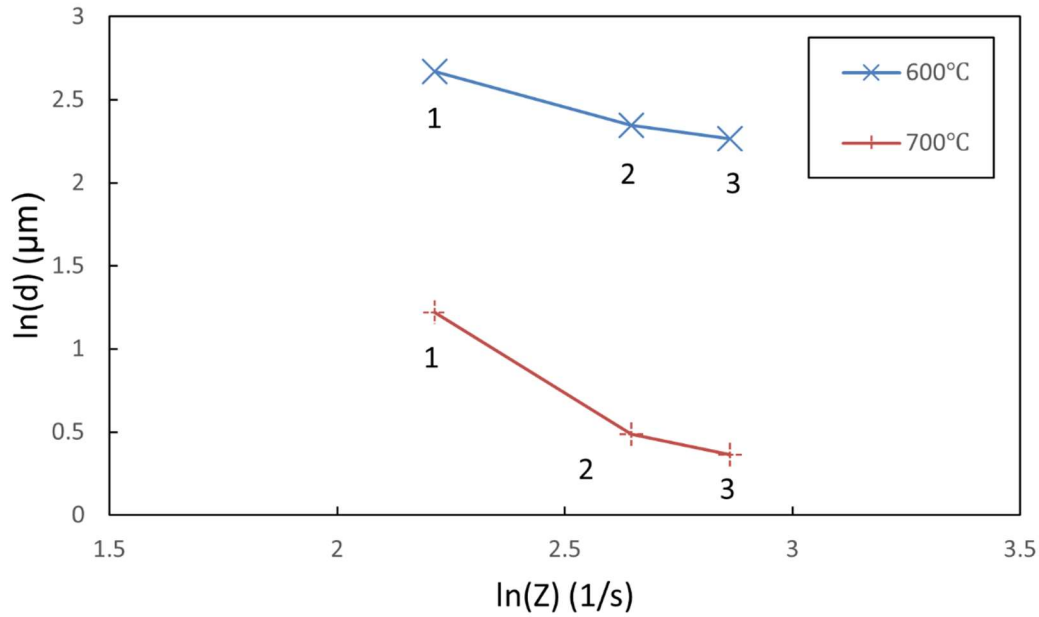


**Figure 20.** Relationship between  $\ln(Z) - \ln(d)$ .

### 5.9. Micro-hardness vs. Z-parameter

The micro-hardness values were collected from the upper, centre, and lower region samples, with positions from the upper edge to the lower edge to demonstrate the relation between micro-hardness and Z-parameter. The strain rate values were obtained from step-down nodes on the element thickness surface to correspond to each micro-hardness value. Z-parameter values were calculated based using Eq. (12). Hence, applying the natural logarithm on Z-parameter, the relationship between them is shown in Figure 21.

As indicated, the increase of the Z-parameter leads to an increase in micro-hardness. It is observed that the Z-parameter distribution for all samples is in a low-high-low profile which

agrees with the micro-hardness profile, as shown in Figure 19. The nodes at the upper and lower edge reveal lower micro-hardness and Z values, and the centre nodes reveal higher values. The strain hardening is relatively higher at centre regions than surface edges since the heat is generated from the material centre to the outer surface. Due to the heat loss, the temperature at the surface edges is slightly lower than that at the centre. This is clear evidence that the temperature affects the Z-parameters distribution, and slight variance of temperature ( $\pm 30\text{ }^{\circ}\text{C}$ ) throughout the thickness may induce a noticeable change. By comparing the temperatures, it is noted that  $700^{\circ}\text{C}$  shows higher micro-hardness readings with close Z-parameter values to  $600^{\circ}\text{C}$ . This demonstrates that the DRX at  $700\text{ }^{\circ}\text{C}$  is more pronounced than at  $600\text{ }^{\circ}\text{C}$ , wherein the strong dislocation mobility of grains enhances the micro-hardness of the workpiece. Similar results were reported by (Valoppi et al., 2016) on electric heating SPIF, which concluded that the higher temperature initiates higher strain hardening that enhances the stretching mechanism. The temperature releasing strong internal stresses that induces an annealing phenomenon on the workpiece thus induces higher micro-hardness readings.

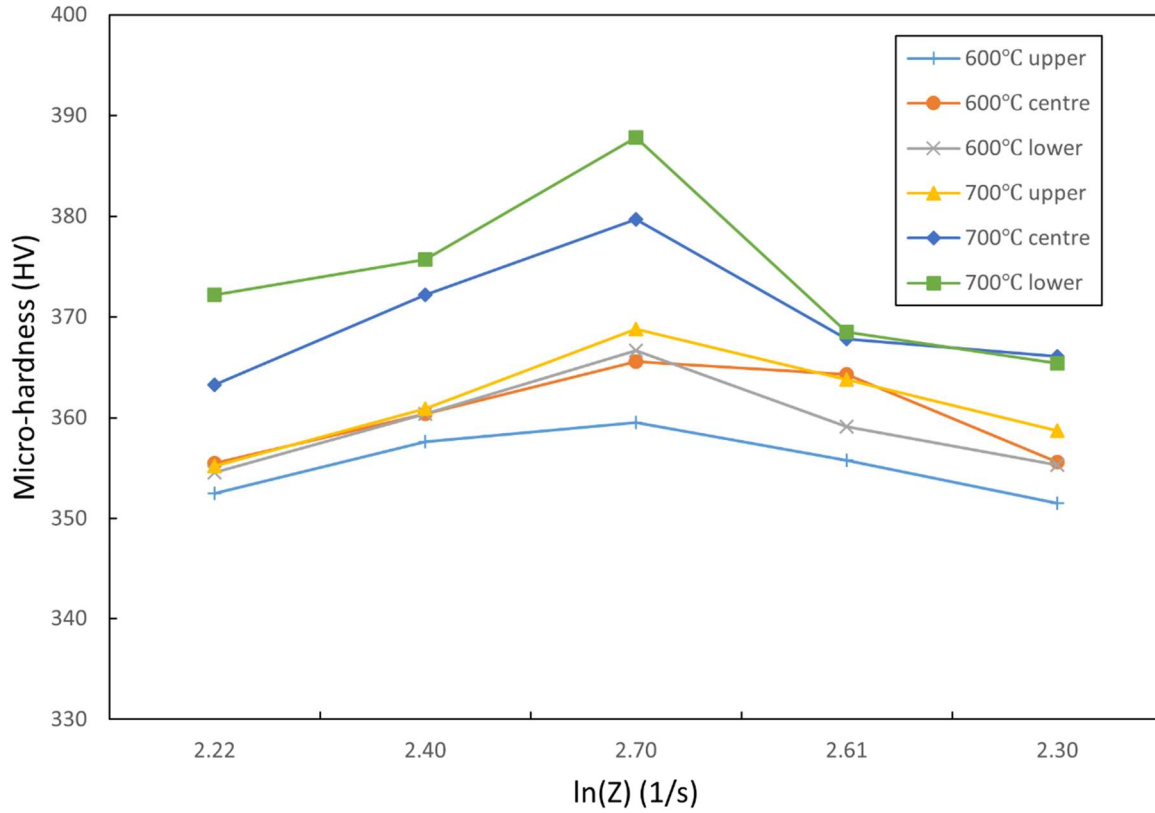


**Figure 21.** Relationship between  $\ln(Z)$  – Microhardness(HV)

## 6. Conclusion

This article has determined the thermal, mechanical, and microstructure properties of the induction heating assisted SPIF process of the Ti-6Al-4V alloy sheet. The performance is significantly affected by temperature and its relevant strain rate distribution:

- The Nickel alloy ball-roller tool exhibits high performance to reduce friction and improves geometric accuracy and surface quality.
- Temperature is a key factor that affects geometrical accuracy. At the higher temperature (700 °C), the workpiece is more ductile which enables a lower forming force to deform the material hence achieve better geometrical accuracy.

- The lubricant is dissipating as the forming tool passing through the centre and lower region of the workpiece. Therefore, the surface roughness parameter  $S_a$  is increased. This phenomenon is more pronounced at 700 °C samples °C.
- The  $S_z$  at 600 °C has a peak value at the upper region and is reduced for the centre and lower regions. The opposite trend can be observed at 700 °C due to the dissipation of lubricant.
- The FE model predicts the mechanical properties with a high degree of accuracy. The temperature variations during the experiments as well as the data filtering affect the prediction accuracy.
- SEM and EBSD results reveal an increment of grain refinement for as-received, 600°C and 700 °C samples. The grains slip is more sufficient at 700 °C, which leads to pronounced DRX that generates more isotropic microstructure than at 600°C.
- Z-parameter calculations estimate an inverse proportion between the grain size and Z-parameter. This phenomenon is more pronounced at 700°C, which proves that the higher temperature is more effective in activating strong grains slip and re-orientation.
- The relation between micro-hardness and Z-parameter reveals that the micro-hardness is very sensitive to the temperature, as a slight variation of thermal-straining between the material centre and surface will induce a noticeable change in micro-hardness. The induction heating is more efficient at the material centre, thus resulting in a low-high-low micro-hardness profile.

In the future, lubricants should be studied to improve sustainability in the heat-assisted SPIF process. Uniform temperature supply and constant strain rate are interesting factors to investigate as they affect the homogeneity of Ti-6Al-4V, resulting in different thermal, mechanical, and microstructural properties.

## Acknowledgement

This work was funded by the Department of Mechanical Engineering, University of Birmingham. We thank Dr Chloe Chen for her linguistic assistance during the preparation of this manuscript. A special appreciation to Wanpeng Li from Xinyu Technology Development Company Limited for EBSD samples preparation.

## References

- Al-Obaidi, A., Kräusel, V. & Landgrebe, D., 2016. Hot single-point incremental forming assisted by induction heating. *The International Journal of Advanced Manufacturing Technology* 82, 1163-1171.10.1007/s00170-015-7439-x
- Ambrogio, G., Filice, L. & Gagliardi, F., 2012. Formability of lightweight alloys by hot incremental sheet forming. *Materials & Design* 34, 501-508.10.1016/j.matdes.2011.08.024
- Ambrogio, G., Gagliardi, F., Chamanfar, A., Misiolek, W. Z. & Filice, L. J. T. I. J. o. A. M. T., 2017. Induction heating and cryogenic cooling in single point incremental forming of Ti-6Al-4V: process setup and evolution of microstructure and mechanical properties. *The International Journal of Advanced Manufacturing Technology* 91, 803-812.10.1007/s00170-016-9794-7
- Ammouri, A. H., Kridli, G., Ayoub, G. & Hamade, R. F., 2015. Relating grain size to the Zener–Hollomon parameter for twin-roll-cast AZ31B alloy refined by friction stir processing. *Journal of Materials Processing Technology* 222, 301-306.10.1016/j.jmatprotec.2015.02.037
- Bantounas, I., Dye, D. & Lindley, T. C., 2009. The effect of grain orientation on fracture morphology during high-cycle fatigue of Ti–6Al–4V. *Acta Materialia* 57, 3584-3595.10.1016/j.actamat.2009.04.018
- Cao, T., Lu, B., Xu, D., Zhang, H., Chen, J., Long, H. & Cao, J., 2015. An efficient method for thickness prediction in multi-pass incremental sheet forming. *International Journal of Advanced Manufacturing Technology* 77, 469-483.10.1007/s00170-014-6489-9
- Dai, J., Wang, T., Chai, L., Hu, X., Zhang, L. & Guo, N., 2020. Characterization and correlation of microstructure and hardness of Ti–6Al–4V sheet surface-treated by pulsed laser. *Journal of Alloys and Compounds* 826, 154243.10.1016/j.jallcom.2020.154243
- Davarpanah, M. A., Mirkouei, A., Yu, X., Malhotra, R. & Pilla, S., 2015. Effects of incremental depth and tool rotation on failure modes and microstructural properties in Single Point Incremental Forming of polymers. *Journal of Materials Processing Technology* 222, 287-300.<https://doi.org/10.1016/j.jmatprotec.2015.03.014>
- Desalegn, D., Ramulu, P., Hailu, D., S, S. K., Velmurugan, P. & Devuri, V., 2019. Formability Analyses on Single Point Incremental Sheet Forming Process on Aluminum 1050. *Materials Science Forum* 969, 703-708.10.4028/[www.scientific.net/MSF.969.703](http://www.scientific.net/MSF.969.703)
- Duflou, J. R., Habraken, A. M., Cao, J., Malhotra, R., Bambach, M., Adams, D., Vanhove, H., Mohammadi, A. & Jeswiet, J., 2018. Single point incremental forming: state-of-the-art and prospects. *International Journal of Material Forming* 11, 743-773.10.1007/s12289-017-1387-y

- Essa, K. & Hartley, P., 2009. Numerical simulation of single and dual pass conventional spinning processes. *International Journal of Material Forming* 2, 271.10.1007/s12289-009-0602-x
- Essa, K. & Hartley, P., 2011. An assessment of various process strategies for improving precision in single point incremental forming. *International Journal of Material Forming* 4, 401-412.10.1007/s12289-010-1004-9
- Fan, G., Sun, F., Meng, X., Gao, L. & Tong, G., 2010. Electric hot incremental forming of Ti-6Al-4V titanium sheet. *The International Journal of Advanced Manufacturing Technology* 49, 941-947.10.1007/s00170-009-2472-2
- Gatea, S., Lu, B., Chen, J., Ou, H. & McCartney, G., 2019. Investigation of the effect of forming parameters in incremental sheet forming using a micromechanics based damage model. *International Journal of Material Forming* 12, 553-574.10.1007/s12289-018-1434-3
- Gatea, S., Ou, H., Lu, B. & McCartney, G., 2017. Modelling of ductile fracture in single point incremental forming using a modified GTN model. *Engineering Fracture Mechanics* 186, 59-79.10.1016/j.engfracmech.2017.09.021
- Göttmann, A., Bailly, D., Bergweiler, G., Bambach, M., Stollenwerk, J., Hirt, G. & Loosen, P., 2012. A novel approach for temperature control in ISF supported by laser and resistance heating. *The International Journal of Advanced Manufacturing Technology* 67, 2195-2205.10.1007/s00170-012-4640-z
- Guan, D., Rainforth, W. M., Gao, J., Ma, L. & Wynne, B., 2018. Individual effect of recrystallisation nucleation sites on texture weakening in a magnesium alloy: Part 2-shear bands. *Acta Materialia* 145, 399-412.10.1016/j.actamat.2017.12.019
- Honarparisheh, M., Abdolhoseini, M. J. & Amini, S., 2015. Experimental and numerical investigation of the hot incremental forming of Ti-6Al-4V sheet using electrical current. *The International Journal of Advanced Manufacturing Technology* 83, 2027-2037.10.1007/s00170-015-7717-7
- Huang, L., Yang, H., Zhan, M. & Hu, L.-j., 2008. Numerical simulation of influence of material parameters on splitting spinning of aluminum alloy. *Transactions of Nonferrous Metals Society of China* 18, 674-681.10.1016/s1003-6326(08)60117-x
- Hussain, G. & Gao, L., 2007. A novel method to test the thinning limits of sheet metals in negative incremental forming. *International Journal of Machine Tools and Manufacture* 47, 419-435.<https://doi.org/10.1016/j.ijmachtools.2006.06.015>
- Hussain, G., Gao, L., Hayat, N., Cui, Z., Pang, Y. C. & Dar, N. U., 2008. Tool and lubrication for negative incremental forming of a commercially pure titanium sheet. *Journal of Materials Processing Technology* 203, 193-201.<https://doi.org/10.1016/j.jmatprotec.2007.10.043>
- Iseki, H. & Naganawa, T., 2002. Vertical wall surface forming of rectangular shell using multistage incremental forming with spherical and cylindrical rollers. *Journal of Materials Processing Technology* 130-131, 675-679.10.1016/s0924-0136(02)00735-5
- Kotkunde, N., Deole, A. D., Gupta, A. K. & Singh, S. K., 2014. Comparative study of constitutive modeling for Ti-6Al-4V alloy at low strain rates and elevated temperatures. *Materials & Design* 55, 999-1005.10.1016/j.matdes.2013.10.089
- Kumar, A., Gulati, V., Kumar, P., Singh, V., Kumar, B. & Singh, H., 2019. Parametric effects on formability of AA2024-O aluminum alloy sheets in single point incremental forming. *Journal of Materials Research and Technology* 8, 1461-1469.10.1016/j.jmrt.2018.11.001
- Lee, W.-S. & Lin, C.-F., 1998. High-temperature deformation behaviour of Ti6Al4V alloy evaluated by high strain-rate compression tests. *Journal of Materials Processing Technology* 75, 127-136.10.1016/s0924-0136(97)00302-6

- Liu, R., Lu, B., Xu, D., Chen, J., Chen, F., Ou, H. & Long, H., 2016. Development of novel tools for electricity-assisted incremental sheet forming of titanium alloy. *The International Journal of Advanced Manufacturing Technology* 85, 1137-1144.10.1007/s00170-015-8011-4
- Lu, B., Fang, Y., Xu, D. K., Chen, J., Ai, S., Long, H., Ou, H. & Cao, J., 2015. Investigation of material deformation mechanism in double side incremental sheet forming. *International Journal of Machine Tools and Manufacture* 93, 37-48.10.1016/j.ijmachtools.2015.03.007
- Moser, N., Pritchett, D., Ren, H., Ehmann, K. F. & Cao, J., 2016. An efficient and general finite element model for double-sided incremental forming. *Journal of Manufacturing Science and Engineering, Transactions of the ASME* 138.10.1115/1.4033483
- Najafabady, S. A. & Ghaei, A., 2016. An experimental study on dimensional accuracy, surface quality, and hardness of Ti-6Al-4 V titanium alloy sheet in hot incremental forming. *The International Journal of Advanced Manufacturing Technology* 87, 3579-3588.10.1007/s00170-016-8712-3
- Nemat-Nasser, S., Guo, W.-G., Nesterenko, V. F., Indrakanti, S. S. & Gu, Y.-B., 2001. Dynamic response of conventional and hot isostatically pressed Ti-6Al-4V alloys: experiments and modeling. *Mechanics of Materials* 33, 425-439.10.1016/s0167-6636(01)00063-1
- Niessen, F., Nyssönen, T., Gazder, A. A. & Hielscher, R., 2021. Parent grain reconstruction from partially or fully transformed microstructures in MTEX. *arXiv preprint arXiv:2104.14603*
- Orozco-Caballero, A., Li, F., Esqué-de los Ojos, D., Atkinson, M. D. & Quinta da Fonseca, J., 2018. On the ductility of alpha titanium: The effect of temperature and deformation mode. *Acta Materialia* 149, 1-10.10.1016/j.actamat.2018.02.022
- Ortiz, M., Penalva, M., Iriondo, E. & Lacalle, L., 2019. Accuracy and Surface Quality Improvements in the Manufacturing of Ti-6Al-4V Parts Using Hot Single Point Incremental Forming. *Metals - Open Access Metallurgy Journal* 9, 697.10.3390/met9060697
- Ortiz, M., Penalva, M., Iriondo, E. & López de Lacalle, L. N., 2020. Investigation of Thermal-Related Effects in Hot SPIF of Ti-6Al-4V Alloy. *International Journal of Precision Engineering and Manufacturing-Green Technology* 7, 299-317.10.1007/s40684-019-00038-z
- Qu, S. J., Tang, S. Q., Feng, A. H., Feng, C., Shen, J. & Chen, D. L., 2018. Microstructural evolution and high-temperature oxidation mechanisms of a titanium aluminide based alloy. *Acta Materialia* 148, 300-310.10.1016/j.actamat.2018.02.013
- Sabat, R. K., Surya Pavan, M. V. S. D. S., Aakash, D. S., Kumar, M. & Sahoo, S. K., 2018. Mechanism of texture and microstructure evolution during warm rolling of Ti-6Al-4V alloy. *Philosophical Magazine* 98, 2562-2581.10.1080/14786435.2018.1493237
- Satko, D. P., Shaffer, J. B., Tiley, J. S., Semiatin, S. L., Pilchak, A. L., Kalidindi, S. R., Kosaka, Y., Glavicic, M. G. & Salem, A. A., 2016. Effect of microstructure on oxygen rich layer evolution and its impact on fatigue life during high-temperature application of  $\alpha/\beta$  titanium. *Acta Materialia* 107, 377-389.10.1016/j.actamat.2016.01.058
- Shrivastava, P. & Tandon, P., 2018. Microstructure and texture based analysis of forming behavior and deformation mechanism of AA1050 sheet during Single Point Incremental Forming. *Journal of Materials Processing Technology* 266.10.1016/j.jmatprotec.2018.11.012

- Smith, J., Liu, W. K. & Cao, J., 2015. A general anisotropic yield criterion for pressure-dependent materials. *International Journal of Plasticity* 75, 2-21.10.1016/j.ijplas.2015.08.009
- Tabei, A., Abed, F. H., Voyiadjis, G. Z. & Garmestani, H., 2017. Constitutive modeling of Ti-6Al-4V at a wide range of temperatures and strain rates. *European Journal of Mechanics - A/Solids* 63, 128-135.10.1016/j.euromechsol.2017.01.005
- Tolipov, A., Elghawail, A., Abosaf, M., Pham, D., Hassanin, H. & Essa, K., 2019. Multipoint forming using mesh-type elastic cushion: modelling and experimentation. *The International Journal of Advanced Manufacturing Technology* 103, 2079-2090.10.1007/s00170-019-03635-z
- Valoppi, B., Sánchez Egea, A. J., Zhang, Z., González Rojas, H. A., Ghiotti, A., Bruschi, S. & Cao, J., 2016. A hybrid mixed double-sided incremental forming method for forming Ti6Al4V alloy. *CIRP Annals - Manufacturing Technology* 65, 309-312.10.1016/j.cirp.2016.04.135
- Wang, C., Yu, D., Niu, Z., Zhou, W., Chen, G., Li, Z. & Fu, X., 2020. The role of pyramidal  $\langle c + a \rangle$  dislocations in the grain refinement mechanism in Ti-6Al-4V alloy processed by severe plastic deformation. *Acta Materialia*.<https://doi.org/10.1016/j.actamat.2020.08.076>
- Wang, F., Zhao, J., Zhu, N. & Li, Z., 2015. A comparative study on Johnson–Cook constitutive modeling for Ti–6Al–4V alloy using automated ball indentation (ABI) technique. *Journal of Alloys and Compounds* 633, 220-228.10.1016/j.jallcom.2015.01.284
- Weiss, I. & Semiatin, S. L., 1999. Thermomechanical processing of alpha titanium alloys—an overview. *Materials Science and Engineering: A* 263, 243-256.10.1016/s0921-5093(98)01155-1
- Xia, Y.-f., Jiang, W., Cheng, Q., Jiang, L. & Jin, L., 2020. Hot deformation behavior of Ti—6Al—4V—0.1Ru alloy during isothermal compression. *Transactions of Nonferrous Metals Society of China* 30, 134-146.10.1016/s1003-6326(19)65186-1
- Xiao, J., Li, D. S., Li, X. Q. & Deng, T. S., 2012. Constitutive modeling and microstructure change of Ti–6Al–4V during the hot tensile deformation. *Journal of Alloys and Compounds* 541, 346-352.10.1016/j.jallcom.2012.07.048
- Xu, D. K., Lu, B., Cao, T. T., Zhang, H., Chen, J., Long, H. & Cao, J., 2016. Enhancement of process capabilities in electrically-assisted double sided incremental forming. *Materials and Design* 92, 268-280.10.1016/j.matdes.2015.12.009
- Xu, X., Zhang, J., Outeiro, J., Xu, B. & Zhao, W., 2020. Multiscale simulation of grain refinement induced by dynamic recrystallization of Ti6Al4V alloy during high speed machining. *Journal of Materials Processing Technology* 286, 116834.10.1016/j.jmatprotec.2020.116834
- Zherebtsov, S. V., Kudryavtsev, E. A., Salishchev, G. A., Straumal, B. B. & Semiatin, S. L., 2016. Microstructure evolution and mechanical behavior of ultrafine Ti6Al4V during low-temperature superplastic deformation. *Acta Materialia* 121, 152-163.<https://doi.org/10.1016/j.actamat.2016.09.003>